
Sparse Bayesian Deep Functional Learning with Structured Region Selection

Xiaoxian Zhu¹ Yingmeng Li¹ Shuangge Ma² Mengyun Wu¹

Abstract

In modern applications such as ECG monitoring, neuroimaging, wearable sensing, and industrial equipment diagnostics, complex and continuously structured data are ubiquitous, presenting both challenges and opportunities for functional data analysis. However, existing methods face a critical trade-off: conventional functional models are limited by linearity, whereas deep learning approaches lack interpretable region selection for sparse effects. To bridge these gaps, we propose a sparse Bayesian functional deep neural network (sBayFDNN). It learns adaptive functional embeddings through a deep Bayesian architecture to capture complex nonlinear relationships, while a structured prior enables interpretable, region-wise selection of influential domains with quantified uncertainty. Theoretically, we establish rigorous approximation error bounds, posterior consistency, and region selection consistency. These results provide the first theoretical guarantees for a Bayesian deep functional model, ensuring its reliability and statistical rigor. Empirically, comprehensive simulations and real-world studies confirm the effectiveness and superiority of sBayFDNN. Crucially, sBayFDNN excels in recognizing intricate dependencies for accurate predictions and more precisely identifies functionally meaningful regions, capabilities fundamentally beyond existing approaches.

1. Introduction

With rapid technological advances, diverse fields—from healthcare to neuroscience—are generating increasingly complex data that exhibit inherent structure and continuity over time or space. For instance, electrocardiogram (ECG) recordings are analyzed as functional curves to elucidate

cardiac morphology and identify pathological patterns, offering insights into cardiovascular health (Pang et al., 2023). Similarly, neuroimaging data are modeled as spatiotemporal fields to capture brain dynamics constrained by anatomical geometry, advancing the study of neural functions and disorders (Tsai et al., 2024). Such data are naturally viewed as realizations of underlying functions and are suited for analysis within functional data analysis (FDA), which uses their smoothness and structure to model temporal or spatial patterns. The analysis of these functional observations is important, particularly in human health studies, where interpreting such signals can inform diagnosis, monitoring, and treatment.

In FDA, supervised learning with functional predictors is fundamentally important yet faces two major challenges. First, the relationship between functional predictors and responses is often intrinsically complex and nonlinear. Ignoring such nonlinearity risks significant model misspecification, potentially leading to poor predictive performance in real-world applications. Second, and more critically, many applications exhibit local sparsity or region-specific effects. This means the predictive relationship is not globally active across the entire function domain; instead, it is concentrated within one or a few specific, contiguous subregions (e.g., time intervals or wavelength bands) where the functional coefficient is nonzero, while being negligible or zero elsewhere. Failure to account for this structure may introduce substantial noise and degrade both interpretability and estimation efficiency.

These two challenges are commonly intertwined in practice. For example, in bedside monitoring, physiological waveforms such as ECG—driven by intricate and dynamic pathophysiological states—not only manifest highly complex and nonlinear patterns but also frequently exhibit local sparsity (Moor et al., 2023). Specifically, clinically actionable information is not distributed uniformly but is concentrated within physiologically meaningful regions of the waveform, such as the QRS complex for arrhythmia analysis or the ST segment for ischemia detection. Signals from other intervals are often non-informative. This makes interpretable region selection a core enabling step, as it precisely targets the localized subdomains where complex nonlinear relationships are most active and meaningful, thereby forming the foundation for efficient and robust functional models.

¹School of Statistics and Data Science, Shanghai University of Finance and Economics ²Department of Biostatistics, Yale School of Public Health. Correspondence to: Mengyun Wu <wu.mengyun@mail.shufe.edu.cn>.

Supervised learning with functional data has been extensively studied. Classical functional linear regression (FLR) estimates smooth coefficient functions but lacks inherent region selection—a limitation partially mitigated by later sparse FLR variants, though linearity constraints remain. Nonlinear functional models offer flexibility yet often depend on prespecified structures, limiting their capacity to capture highly complex relationships. While deep neural networks (DNNs) provide strong approximation power and have been adapted to functional settings, existing DNN-based methods focus predominantly on prediction and do not incorporate interpretable, structured region selection on the functional domain. Moreover, common DNN feature selection techniques are designed for scalar inputs and fail to leverage the continuous nature of functional data. These gaps underscore the need for a DNN framework that jointly handles nonlinear complexity and performs interpretable region selection in functional settings.

We propose a sparse Bayesian deep neural network (sBayFDNN) that integrates functional embedding learning with a Bayesian DNN architecture to perform interpretable region-wise selection for functional predictors. The model captures flexible nonlinear function-to-scalar relationships while providing posterior inference for uncertainty quantification. Our main contributions are:

- **A Bayesian Functional DNN Framework with Uncertainty Quantification:** We introduce a model that embeds functional predictors through a deep Bayesian network to capture complex nonlinear associations with scalar responses. The framework delivers not only point estimates but also posterior uncertainty, overcoming the rigidity of traditional functional regression.
- **Interpretable Region Selection via Structured Sparsity:** A sparse prior is imposed on the first hidden layer to perform region-wise functional selection. This significantly enhances model interpretability while mitigating the black-box nature of conventional DNNs, yielding actionable insights into influential domains.
- **Theoretical Guarantees:** We establish rigorous theoretical results, including approximation error bounds, posterior consistency, and region selection consistency. These provide the first theoretical foundation for a Bayesian deep functional model, thereby opening a new venue for statistically rigorous and interpretable functional deep learning.
- **Empirical Validation:** Comprehensive simulations and diverse real-world studies confirm that sBayFDNN outperforms existing methods in both prediction accuracy and region identification, especially in challenging scenarios where conventional models are misspecified or inflexible, demonstrating its practical superiority.

2. Related Works

2.1. Classical functional regression methods

Classical functional regression methods, represented by the functional linear model and its extensions, establish relationships between functional predictors and scalar responses using techniques such as B-splines (Cardot et al., 2003), reproducing kernel Hilbert spaces (Crambes et al., 2009), and smoothing regularization (Cai & Yuan, 2012). To enhance interpretability, sparse penalization methods have been introduced for local region selection, including sparse functional linear regression (Lee & Park, 2012), smooth locally sparse estimators (Lin et al., 2017; Belli, 2022), and their Bayesian counterparts (Zhu et al., 2025). To move beyond linearity, nonlinear methods such as functional single-index models have been proposed (Jiang et al., 2020), which can also achieve local sparsity via penalization (Nie et al., 2023).

However, these approaches face key limitations: linear models cannot adequately capture complex nonlinear relationships, while existing nonlinear methods rely on pre-defined kernels or bases, limiting their flexibility and capacity to model intricate dependencies directly from data.

2.2. Deep Learning for Functional Data

Deep learning for functional data has advanced in recent years, with methods primarily aimed at enhancing representation learning and predictive performance. Early approaches introduced adaptive basis layers to learn data-driven functional representations within DNNs (Yao et al., 2021), and were followed by DNNs specifically designed for functional inputs (Thind et al., 2023) and classifiers built on functional principal components (Wang et al., 2023). Autoencoder architectures have also been adapted for functional latent representation learning (Wu et al., 2024).

Despite their predictive power, these methods often operate as “black boxes”, lacking explicit mechanisms for region selection on the functional domain. This limits their utility in scientific applications where identifying which specific regions of the data drive predictions is essential.

2.3. Sparsity and Selection in Neural Networks

A parallel line of research incorporates sparsity into neural networks for vector-valued inputs. This includes frameworks performing variable selection via group sparsity penalties on the first hidden layer (Dinh & Ho, 2020; Chu et al., 2023; Luo & Halabi, 2025), architectures employing sparsity-inducing mechanisms on linear input layers (Chen et al., 2021; Atashgahi et al., 2023), and residual layers used to achieve feature-wise sparsity (Lemhadri et al., 2021; Fan & Waldmann, 2025). Furthermore, Sun et al. (2022) proposed a Bayesian framework to learn sparse DNNs through

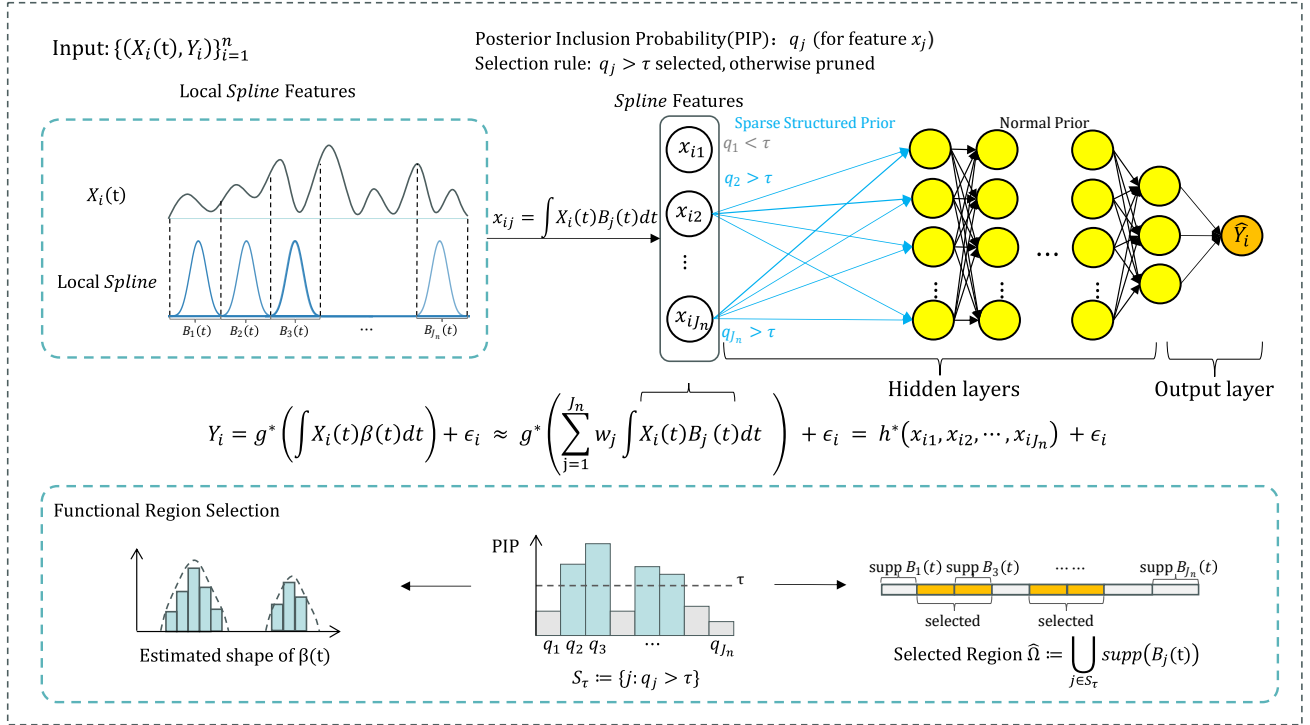


Figure 1. Workflow of sBayFDNN. The functional predictor $X_i(t)$ is projected onto locally supported B-spline bases to form spline features $\mathbf{x}_i = (x_{i1}, \dots, x_{iJ_n})^\top$. A DNN with a spike-and-slab prior on the first-layer weight columns yields feature-wise posterior inclusion probabilities (PIPs) q_j , which are thresholded to select spline features and mapped back to the function domain to produce an estimated active region $\hat{\Omega}$.

connection pruning, establishing posterior consistency but not traditional input-level variable selection. Beyond variable selection, similar sparse DNN techniques have also been developed for applications in other fields, such as biological or social network reconstruction (Fan et al., 2025; Yang et al., 2026).

While these techniques enhance interpretability for vector data, they are not designed to exploit the continuous, structured nature of functional inputs. Consequently, a significant gap remains for a method that integrates nonlinear deep learning with structured, interpretable region selection and uncertainty quantification specifically for functional data.

3. Methodology

Let $X_1(t), \dots, X_n(t)$ be n independent functional covariates defined on the closed interval $\mathcal{T} \subset \mathbb{R}$. For theoretical and computational purposes, \mathcal{T} is standardized to $[0, 1]$. Let Y_i denote a scalar response. We consider a functional single-index model (see Figure 1 for a schematic overview):

$$Y_i = g^* \left(\int_{\mathcal{T}} X_i(t) \beta(t) dt \right) + \varepsilon_i, \quad (1)$$

where $\varepsilon_i \sim \mathcal{N}(0, \sigma_\varepsilon^2)$, $\beta(\cdot)$ is an unknown coefficient function, and $g^*(\cdot)$ is an unknown nonlinear function. Without

loss of generality, we assume the domain of $g^*(\cdot)$ is $[0, 1]$; this can be achieved by suitably rescaling $\int_{\mathcal{T}} X_i(t) \beta(t) dt$ and absorbing the scaling into the definition of g^* . For notational simplicity, we retain the original notation in the subsequent exposition.

The function $g^*(\cdot)$ allows for a flexible, potentially nonlinear relationship between the scalar response and the functional covariate through the single-index projection. Motivated by applications where the association is driven by only a few subregions of \mathcal{T} (e.g., a small number of time intervals), we assume that $\beta(\cdot)$ is effectively localized and aim to identify the corresponding active regions.

To circumvent the infinite-dimensionality of $\beta(\cdot)$, we approximate it using a truncated B-spline basis expansion:

$$\beta_{J_n}(t) = \sum_{j=1}^{J_n} w_{J_n, j} B_j(t), \quad (2)$$

which yields the following finite-dimensional representation:

$$Y_i \approx g^*(\boldsymbol{\eta}(X_i)^\top \mathbf{w}_{J_n}) + \varepsilon_i = h^*(\boldsymbol{\eta}(X_i)) + \varepsilon_i. \quad (3)$$

by replacing $\beta(\cdot)$ with $\beta_{J_n}(\cdot)$, where $\int_{\mathcal{T}} X_i(t) \beta_{J_n}(t) dt = \boldsymbol{\eta}(X_i)^\top \mathbf{w}_{J_n}$. Here, $\{B_j(\cdot)\}_{j=1}^{J_n}$ denotes a collection of J_n B-spline basis functions, and $\mathbf{w}_{J_n} :=$

$(w_{J_n,1}, \dots, w_{J_n,J_n})^\top \in \mathbb{R}^{J_n}$ is the corresponding vector of coefficients. The spline features $\boldsymbol{\eta}(X_i) = (x_{i1}, \dots, x_{iJ_n})^\top \in \mathbb{R}^{J_n}$, where $x_{ij} := \int_{\mathcal{T}} X_i(t) B_j(t) dt$. We further introduce $h^*(\cdot)$, which absorbs the B-spline coefficient vector \boldsymbol{w}_{J_n} , thus reducing the problem to learning a finite-dimensional function.

Next, we aim to estimate $h^*(\cdot)$ using a DNN F_θ that takes $\boldsymbol{\eta}(X_i) \in \mathbb{R}^{J_n}$ as input. The network can be written as

$$F_\theta = A_{H_n} \circ \sigma \circ A_{H_n-1} \circ \dots \circ \sigma \circ A_1. \quad (4)$$

Here, we consider a feedforward DNN with $H_n - 1$ hidden layers and width L_h at layer h , where $L_0 = J_n$ and $L_{H_n} = 1$, with a common activation $\sigma(\cdot)$ in the hidden layers and a linear output layer. We consider the ReLU activation in our study. Let $\theta = \{(\boldsymbol{W}_h, \boldsymbol{b}_h)\}_{h=1}^{H_n}$, where $\boldsymbol{W}_h \in \mathbb{R}^{L_h \times L_{h-1}}$ and $\boldsymbol{b}_h \in \mathbb{R}^{L_h}$ denote the weights and biases. The affine map is defined as $A_h(\boldsymbol{u}) := \boldsymbol{W}_h \boldsymbol{u} + \boldsymbol{b}_h$.

In (3), since the B-spline basis is locally supported, the localization of $\beta(\cdot)$ over \mathcal{T} is naturally reflected in the sparsity pattern of \boldsymbol{w}_{J_n} in (2). Therefore, we consider the setting where \boldsymbol{w}_{J_n} is sparse, so that $\boldsymbol{\eta}(X_i)^\top \boldsymbol{w}_{J_n} = \boldsymbol{\eta}_{S_{J_n}}(X_i)^\top \boldsymbol{w}_{S_{J_n}}$, where $S_{J_n} \subset \{1, \dots, J_n\}$ denotes an unknown support set, $\boldsymbol{\eta}_{S_{J_n}}(X_i)$ and $\boldsymbol{w}_{S_{J_n}}$ denote the corresponding subvectors. With (4), since \boldsymbol{w}_{J_n} is absorbed into $h^*(\cdot)$, the sparsity of \boldsymbol{w}_{J_n} naturally translates into sparsity of the first-layer weight matrix $\boldsymbol{W}_1 \in \mathbb{R}^{L_1 \times J_n}$. Specifically, denoting by $\boldsymbol{W}_{1,*j} \in \mathbb{R}^{L_1}$ the j -th column of \boldsymbol{W}_1 , we have that if $\|\boldsymbol{W}_{1,*j}\|_2 \neq 0$, then $j \in S_{J_n}$.

Based on (3) and (4), we propose a sparse Bayesian functional DNN (sBayFDNN) framework, employing the following prior distributions for the model parameters:

for $j \in \{1, \dots, J_n\}$,

$$\boldsymbol{W}_{1,*j} \mid \gamma_j \sim \left[\mathcal{N}(0, \sigma_{1,n}^2 \boldsymbol{I}) \right]^{\gamma_j} \left[\mathcal{N}(0, \sigma_{0,n}^2 \boldsymbol{I}) \right]^{1-\gamma_j} \quad (5)$$

$$\pi(\gamma_j) \sim \text{Bern}(\lambda_n), \quad (6)$$

$$\boldsymbol{W}_{h,ab} \sim \mathcal{N}(0, \sigma^2), \quad \forall h \in \{2, \dots, H_n\}, \quad (7)$$

$$\boldsymbol{b}_{h,a} \sim \mathcal{N}(0, \sigma^2), \quad \forall h \in \{1, \dots, H_n\}. \quad (8)$$

Here, $\mathcal{N}(c, d)$ denotes the normal distribution with mean c and variance (covariance) d , and $\text{Bern}(\lambda_n)$ denotes the Bernoulli distribution with success probability $\lambda_n \in (0, 1)$. The symbol \boldsymbol{I} represents an identity matrix of appropriate dimensions. The entry $\boldsymbol{W}_{h,ab}$ corresponds to the (a, b) -th element of the matrix \boldsymbol{W}_h , where $a \in 1, \dots, L_h$ and $b \in 1, \dots, L_{h-1}$. Each γ_j (for $j \in 1, \dots, J_n$) is a binary indicator. We set $\sigma_{1,n}^2 > \sigma_{0,n}^2 > 0$, with $\sigma_{0,n}^2$ taken to be a small positive value, and let $\sigma^2 > 0$.

As introduced above, distinct priors are specified for the first layer and the subsequent layers. To enable functional region selection in the spline-feature domain, we impose a group-wise continuous spike-and-slab prior on each $\boldsymbol{W}_{1,*j}$

for $j = 1, \dots, J_n$. When $\gamma_j = 0$, the spike variance $\sigma_{0,n}^2$ strongly shrinks all entries of $\boldsymbol{W}_{1,*j}$ toward zero with high probability; when $\gamma_j = 1$, the slab variance $\sigma_{1,n}^2$ permits the entries to take appreciable nonzero values, thereby allowing the corresponding spline-basis feature to contribute to the functional representation. For the remaining layers, weights and biases are assigned entrywise independent Gaussian priors $\mathcal{N}(0, \sigma^2)$, which preserves the flexibility needed in the hidden layers to learn complex, nonlinear patterns based on the features identified by the first hidden layer.

4. Optimization-based Bayesian Inference

The proposed Bayesian inference proceeds via three steps: (i) compute a (local) posterior mode (MAP) of the network parameters under the marginal prior; (ii) derive feature-level posterior inclusion probabilities from the first-layer; and (iii) map the selected spline features to an estimated active region. The detailed procedure is described below, and the hyperparameter settings are provided in the Appendix.

4.1. MAP fitting

For θ , we optimize the marginal posterior in which the inclusion indicators γ are integrated out, and denote the resulting marginal prior by $\pi(\theta)$. Then, we compute a MAP by minimizing the negative log-posterior objective

$$\hat{\theta} \in \arg \min_{\theta} \frac{1}{2\sigma_\varepsilon^2} \sum_{i=1}^n \left(Y_i - f_\theta(\boldsymbol{\eta}(X_i)) \right)^2 - \log \pi(\theta), \quad (9)$$

where f_θ is the H_n -layer feedforward network defined in (4). Optimization is carried out using stochastic gradient methods (see Appendix for the detailed algorithm).

4.2. MAP plug-in posterior inclusion probabilities

Denote $A_{1,n} = \lambda_n (\sigma_{1,n}^2)^{-L_1/2}$ and $A_{0,n} = (1 - \lambda_n) (\sigma_{0,n}^2)^{-L_1/2}$. Then, for each feature index j , applying Bayes' rule to (5) and (6) gives the conditional posterior inclusion probability (PIP): $\Pr(\gamma_j = 1 \mid \boldsymbol{W}_{1,*j}) =$

$$\frac{A_{1,n} \exp\left(-\frac{\|\boldsymbol{W}_{1,*j}\|_2^2}{2\sigma_{1,n}^2}\right)}{A_{1,n} \exp\left(-\frac{\|\boldsymbol{W}_{1,*j}\|_2^2}{2\sigma_{1,n}^2}\right) + A_{0,n} \exp\left(-\frac{\|\boldsymbol{W}_{1,*j}\|_2^2}{2\sigma_{0,n}^2}\right)}.$$

We compute plug-in PIP $\hat{q}_j := \Pr(\gamma_j = 1 \mid \hat{\boldsymbol{W}}_{1,*j})$ based on the MAP estimate $\hat{\theta}$ and select spline features by thresholding: $\hat{S}_\tau := \{j : \hat{q}_j > \tau\}$ with default $\tau = 1/2$. Since \hat{q}_j is monotone in $\|\hat{\boldsymbol{W}}_{1,*j}\|_2^2$, this rule is equivalent to thresholding the first-layer column norms.

4.3. Mapping selected features to an active region on \mathcal{T}

Given $\hat{S}_\tau \subset \{1, \dots, J_n\}$, we map the selected spline features back to the functional domain using the local support

of B-splines. Let $\text{supp}(B_j(t)) \subset \mathcal{T}$ denote the support of the j th basis function. We define the estimated active region as $\hat{\Omega} := \bigcup_{j \in \hat{S}_\tau} \text{supp}(B_j)$, and represent $\hat{\Omega}$ as a union of disjoint subintervals by merging adjacent components.

5. Theoretical Properties

Let β^* and $\beta_{J_n}^*$ be the true coefficient function and its truncated counterpart, respectively. Let $\omega_{J_n}^* \in \mathbb{R}^{J_n}$ be the vector of true basis coefficients for $\beta_{J_n}^*$, $S_{J_n}^* = \text{supp}(\omega_{J_n}^*)$ its support, and $s_n = |S_{J_n}^*|$ the sparsity level. Define $e_j^* = \mathbb{I}(j \in S_{J_n}^*)$ as the true binary selection indicator and $\Omega^* \subset \mathcal{T}$ as the true non-zero region of β^* . Denote $\Omega^*(\kappa) = \{t \in \mathcal{T} : |\beta^*(t)| > \kappa\}$ as the strong-signal region and $\Omega^*(\kappa)^c$ as its complement. Denote $a_n \lesssim b_n$ if $a_n \leq Cb_n$ for some constant $C > 0$, and $a_n \asymp b_n$ if $c b_n \leq a_n \leq C b_n$ for constants $0 < c < C$.

Denote $\mu^*(X) = g^*(\int_{\mathcal{T}} X(t)\beta^*(t)dt)$ as the true mean function and $\mu_{\theta}(X) := F_{\theta}(\eta(X))$ as the network output defined in (4). Consider the class of fully-connected, J_n -input ReLU networks, denoted by $\mathcal{NN}_{J_n}(H_n, \bar{L}, E_n)$, with depth H_n , constant maximum hidden width $\bar{L} = \max_{2 \leq k \leq H_n} L_k$, and parameter bound $\|\theta\|_{\infty} \leq E_n$. We define the column-wise support of the network parameters as $\text{supp}_{\text{col}}(\theta) = \{j \in \{1, \dots, J_n\} : \|\mathbf{W}_{1,*j}\|_2 > 0\}$. For any subset $T \subset \{1, \dots, J_n\}$, the associated column-sparse network class is defined as $\mathcal{NN}_{J_n}^{\text{col}}(T; H_n, \bar{L}, E_n) := \{F_{\theta} \in \mathcal{NN}_{J_n}(H_n, \bar{L}, E_n) : \text{supp}_{\text{col}}(\theta) = T\}$.

The following assumptions are imposed.

Assumption 5.1. $\sup_{X_i \in \mathcal{X}} \int_{\mathcal{T}} |X_i(t)| dt \leq C_X$, where \mathcal{X} denotes the function space to which $X_i(t)$ belongs, and C_X is a positive constant.

Assumption 5.2. $\beta^*(t) \in \mathcal{H}^{\alpha_{\beta}}([0, 1])$ for some $\alpha_{\beta} > 0$, where $\mathcal{H}^{\alpha}(I)$ denotes the Hölder space of functions on an interval I with smoothness order α . Ω^* is a finite union of intervals and $|\Omega^*(\kappa_{J_n})^c| \rightarrow 0$, as $n \rightarrow \infty$, with $\kappa_{J_n} = c_{\kappa} C_{\beta} J_n^{-\alpha_{\beta}}$, where $c_{\kappa} > 4$ and C_{β} are constants defined in Lemma B.1 (Appendix). Moreover, the strong-signal region has proportional size in the sense that $\frac{|\Omega^*(\kappa_{J_n})|}{|\Omega^*|} \geq c_{\Omega}$ for some constant $c_{\Omega} \in (0, 1]$ and all sufficiently large n .

Assumption 5.3. $g^*(\cdot) \in \mathcal{H}^{\alpha_g}([0, 1])$ for some constant $\alpha_g > 0$.

These are standard regularity conditions in functional data analysis (Cai & Yuan, 2012; Nie et al., 2023). Assumption 5.1 ensures the well-posedness of the problem by uniformly bounding the predictor trajectories. Assumption 5.2 imposes Hölder smoothness on β^* , guaranteeing its accurate spline approximation. We further assume the active region Ω^* is not overly complex, which excludes highly fragmented supports and aligns with typical domain-selection interpretations. Crucially, we require that the strong-signal region

essentially covers Ω^* up to a negligible set; this acts as a minimum-signal condition in the functional setting, ensuring that the nonzero part of β^* is detectable enough to translate basis selection into faithful support recovery on the domain. We further focus on the practically common proportional sparsity regime, where the strong-signal region retains a non-vanishing fraction of the active domain, which, under locally supported spline bases, implies that the number of active groups scales as $s_n \asymp J_n$. Assumption 5.3 similarly enforces smoothness on the nonparametric link function, thereby supporting stable estimation.

Theorem 5.4. *Suppose that Assumptions 5.1–5.3 hold. Then:*

- (i) *There exists a network parameter vector θ such that:*

$$F_{\theta} = F \in \mathcal{NN}_{J_n}^{\text{col}}(S_{J_n}^*; H_n, \bar{L}, E_n),$$

- (ii) *With $\alpha_1 = \min(\alpha_g, 1)$,*

$$\sup_{X \in \mathcal{X}} |\mu_{\theta}(X) - \mu^*(X)| \lesssim H_n^{-2\alpha_1} + J_n^{-\alpha_{\beta}\alpha_1}.$$

Theorem 5.4 establishes that the true sparse model structure is exactly representable within the proposed architecture (i) and provides a non-asymptotic error bound (ii). This bound guarantees that the approximation error decays to zero as the network depth H_n and the number of spline bases J_n grow, with the rates governed by the smoothness of both the functional coefficient $\beta(t)$ and the link function $g^*(\cdot)$.

Assumption 5.5. For some constants $\tau' > 0$ and $\alpha_{\sigma} > 0$: $\lambda_n \lesssim \frac{1}{J_n [(n\bar{L})^{H_n} (J_n+1)L_1]^{\tau'}}$, $\frac{E_n^2}{H_n(\log n + \log \bar{L})} \lesssim \sigma_{1,n}^2 \lesssim n^{\alpha_{\sigma}}$, and $\frac{E_n^2}{H_n(\log n + \log \bar{L})} \lesssim \sigma^2$.

Assumption 5.6. The DNN F_{θ} in (4) satisfies: $\bar{L} \asymp L_1 \asymp 1$, $H_n \asymp \min\{J_n^{\alpha_{\beta}/2}, s_n\}$ with $s_n \asymp J_n$, and $\|\theta\|_{\infty} \leq E_n$, where $E_n = n^{c_1}$ for some positive constant c_1 .

Assumption 5.5 specifies the rates for key hyperparameters in the Bayesian framework, ensuring the prior is sufficiently diffuse to permit effective posterior contraction toward the true parameter, a standard requirement in Bayesian theory (Ghosal et al., 2000). Assumption 5.6 links the network depth H_n to the sparsity level s_n so that architectural growth respects the intrinsic sparse structure. Similar conditions are commonly adopted in related theoretical analyses.

Let $\Pi(A \mid D_n)$ denote the posterior probability of an event A given the observed data $D_n = \{(X_i, Y_i)\}_{i=1}^n$. Let $p_{\mu^*}(\cdot \mid X)$ be the true conditional density of Y given X , $p_{\mu_{\theta}}(\cdot \mid X)$ be the approximate density induced by the finite-dimensional representation (3) and the sparse DNN defined in (4), and $d(\cdot, \cdot)$ denote the Hellinger distance.

Theorem 5.7. *Suppose that Assumptions 5.1–5.6 hold and there exists an error sequence ε_n^2 satisfying $\varepsilon_n^2 \lesssim \frac{s_n \log(J_n/s_n)}{n} + \frac{s_n (H_n \log n + \log J_n)}{n} + \left(H_n^{-2\alpha_1} + J_n^{-\alpha_\beta \alpha_1} \right)^2$ such that $\sigma_{0,n}^2 \leq \tilde{M}_{n,1}(\varepsilon_n)$ and $\max\{\sigma^2, \sigma_{0,n}^2, \sigma_{1,n}^2\} \leq \tilde{M}_{n,2}(\varepsilon_n)$, where $\tilde{M}_{n,1}(\varepsilon_n)$ and $\tilde{M}_{n,2}(\varepsilon_n)$ are defined in (18) and (19) of Appendix. Then, for some constant $c > 0$, we have*

$$\begin{aligned} P\left[\Pi\{d(p_{\mu_\theta}, p_{\mu^*}) > 4\varepsilon_n \mid D_n\} \geq 2 \exp(-cn\varepsilon_n^2)\right] \\ \leq 2 \exp(-cn\varepsilon_n^2), \end{aligned}$$

and

$$\mathbb{E}\left[\Pi\{d(p_{\mu_\theta}, p_{\mu^*}) > 4\varepsilon_n \mid D_n\}\right] \leq 4 \exp(-2cn\varepsilon_n^2).$$

Theorem 5.7 establishes the posterior contraction rate ε_n of sBayFDNN. This result implies that, with high probability, the posterior distribution concentrates around the true data-generating process at rate ε_n . Specifically, if $\alpha_\beta \leq 2$, then $H_n \asymp J_n^{\alpha_\beta/2}$, setting $J_n \asymp \left(\frac{n}{\log n}\right)^{\frac{1}{1+\alpha_\beta/2+2\alpha_\beta\alpha_1}}$ yields $\varepsilon_n^2 \asymp \left(\frac{\log n}{n}\right)^{\frac{2\alpha_\beta\alpha_1}{1+\alpha_\beta/2+2\alpha_\beta\alpha_1}}$. If $\alpha_\beta > 2$, then $H_n \asymp s_n$, taking $J_n \asymp \left(\frac{n}{\log n}\right)^{\frac{1}{2+4\alpha_1}}$ leads to $\varepsilon_n^2 \asymp \left(\frac{\log n}{n}\right)^{\frac{2\alpha_1}{1+2\alpha_1}}$. Further, define the structural difference as

$$\rho_n(\varepsilon_n) := \max_{1 \leq j \leq J_n} \mathbb{E}\left[|\gamma_j - e_j^*| \cdot \mathbb{I}\{\theta \notin A_n(\varepsilon_n)\} \mid D_n\right],$$

where $\mathbb{E}(\cdot \mid D_n)$ is the conditional expectation, and $A_n(\varepsilon_n) = \{\theta : d(p_{\mu_\theta}, p_{\mu^*}) \geq \varepsilon_n\}$.

Assumption 5.8. $\rho_n(4\varepsilon_n) \rightarrow 0$ as $n \rightarrow \infty$ and $\varepsilon_n \rightarrow 0$.

Assumption 5.8 serves as an identifiability condition. It implies that as $n \rightarrow \infty$ and $\varepsilon_n \rightarrow 0$, any candidate model that is close to the true data-generating process in terms of Hellinger distance must asymptotically share the same underlying structure, thereby guaranteeing the consistent selection (Sun et al., 2022).

Theorem 5.9. *Suppose Assumptions 5.1–5.8 hold. Then:*

- (i) $\max_{1 \leq j \leq J_n} |\hat{q}_j - e_j^*| \xrightarrow{P} 0$.
- (ii) $P(S_{J_n}^* \subset \hat{S}_\tau) \rightarrow 1$ for any prespecified $\tau \in (0, 1)$.
- (iii) $P(\hat{S}_{1/2} = S_{J_n}^*) \rightarrow 1$.
- (iv) $|\hat{\Omega} \Delta \Omega^*| \xrightarrow{P} 0$.

Theorem 5.9 establishes the asymptotic consistency of spline feature selection based on MAP plug-in posterior probabilities, showing that the estimated selection probabilities converge to the true binary indicators. Furthermore, it

guarantees the asymptotically exact recovery of the nonzero region in the continuous function domain from its discrete coefficient support, thereby achieving exact structural selection for the functional effect.

6. Experiments

We evaluate sBayFDNN on synthetic and real-world functional data against five competitors: (1) FNN, a spline-feature-based feedforward network using truncated basis expansion (Thind et al., 2023); (2) AdaFNN, which learns adaptive basis functions via auxiliary networks (Yao et al., 2021); (3) cFuSIM, a functional single-index method with localized regularization (Nie et al., 2023); (4) BFRS, a Bayesian functional region selector with neighborhood structure (Zhu et al., 2025); and (5) SLoS, a functional linear estimator with local sparsity via an fSCAD penalty (Lin et al., 2017). Predictive RMSE is reported for all methods; region-recovery metrics (Recall, Precision, F1) are provided only for sBayFDNN, cFuSIM, BFRS, and SLoS, as FNN and AdaFNN do not perform region selection.

6.1. Simulation Studies

Our simulation studies vary three key aspects: (1) the true coefficient function $\beta^*(t)$, which spans a single interior bump (Simple), a boundary bump (Medium), and a pair of narrow oscillating peaks (Complex); (2) the link function g^* , taken as linear, logistic, sinusoidal, or a composite nonlinear form; and (3) the response signal-to-noise ratio (SNR), set to 5 or 10. Functional covariates are generated from a truncated cosine basis, observed on a discrete grid with added measurement noise (see Appendix for full details).

Figure 2 summarizes region-recovery performance (F1 score) across all simulation scenarios (see Appendix for Recall and Precision). sBayFDNN consistently achieves high mean F1 with tight interquartile ranges, demonstrating robust and stable region identification across both linear and nonlinear regimes. Its advantage is more pronounced in more challenging scenarios with lower signal-to-noise ratios, as well as under harder localization regimes and complex nonlinear link functions g^* . By contrast, several baselines exhibit increased dispersion and more frequent low-F1 outcomes as moves away from central support or g^* departs from linearity.

The distributions also suggest different selection behaviors across methods. For example, cFuSIM often returns broader active regions (capturing truly active intervals but at the cost of more false positives), whereas linear region-selection baselines deteriorate under strong nonlinearity due to model misspecification. In contrast, sBayFDNN maintains a better balance between recall and precision. Beyond aggregate metrics, we further evaluate uncertainty quantification. Tak-

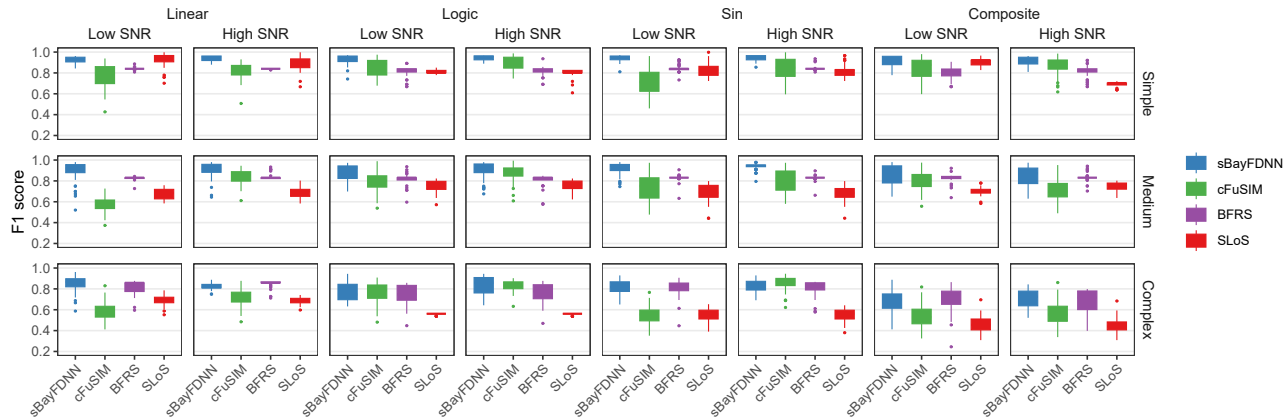


Figure 2. F1 scores across g functions, SNR settings, and $\beta(t)$ scenarios.

ing the high-SNR, Medium- β , logistic-link scenario as an example, Figure 3 presents the posterior selection probabilities from sBayFDNN. These probabilities closely align with the true coefficient function, demonstrating the model’s capacity to effectively capture selection uncertainty.

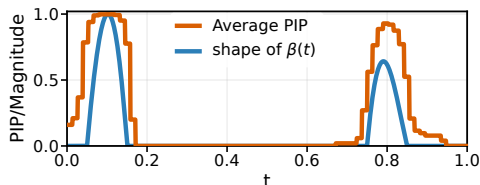


Figure 3. PIPs from sBayFDNN in the high-SNR, Medium- β , logistic-link scenario.

Figure 4 shows that sBayFDNN achieves the lowest or near-lowest mean RMSE in most scenarios, with concentrated distributions, indicating that region interpretability does not come at the cost of predictive performance. Its advantage is most evident under nonlinear links, where flexible function approximation is crucial. Here, sBayFDNN substantially outperforms the spline-based FNN, matches the accuracy of AdaFNN with greater stability, and surpasses cFuSIM when nonlinearity is pronounced. Linear methods (BFRS, SLoS) remain competitive only under nearly linear settings, with performance degrading sharply as nonlinearity increases.

Together, these results affirm the sBayFDNN framework: structured sparsity in the first layer supports interpretable region identification with inherent uncertainty quantification, while subsequent deep layers furnish the flexibility needed for accurate nonlinear prediction.

6.2. Real data analysis

We evaluate our method on four benchmark datasets: ECG, Tecator, Bike rental, and IHPC, using their official

train/validation/test splits throughout. In the ECG task, Lead-II signals are used as functional inputs to predict the QRS duration—a clinically informative measure of ventricular depolarization relevant for detecting conduction abnormalities (Hummel et al., 2009; Kashani & Barold, 2005). For the Tecator dataset, near-infrared absorbance spectra of meat samples serve as functional inputs to predict water content (Thodberg, 2015). In the Bike rental forecasting task (Fanaee-T, 2013), the daily rental-demand profile (a 24-point curve) is used to predict total rentals over the following 7 days. For the IHPC dataset (Hebrail & Berard, 2006), daily minute-averaged active-power trajectories are taken as functional inputs to predict the next-day total energy usage. We report standard predictive metrics (RMSE/MAE) for all datasets. For ECG and Tecator, silver-standard region annotations are available, allowing us to also evaluate region-identification metrics. Detailed data information are provided in the Appendix.

As shown in Table 1 and 2, sBayFDNN delivers the strongest overall performance across all datasets. While all methods attain relatively low precision in region selection, sBayFDNN achieves substantially higher recall and F1. Figure 5 plots the estimated PIPs on the original domains with sBayFDNN for ECG and Tecator. For ECG, sBayFDNN assigns higher inclusion strength within and near the clinically motivated QRS interval (shaded), with PIP values approaching 1 close to the boundaries, consistent with the fact that duration is determined by onset/offset timing and thus endpoint morphology is most informative. For Tecator, the PIP increases within the predefined water band (965–985 nm; shaded), while additional elevated PIP regions appear at earlier wavelengths (including ~ 930 nm, often regarded as lipid/fat-associated in short-wave NIR), plausibly reflecting strong collinearity/compositional coupling between water and fat and other broad predictive structure. These results demonstrate that sBayFDNN can recover physically interpretable regions without sacrificing predictive accuracy.

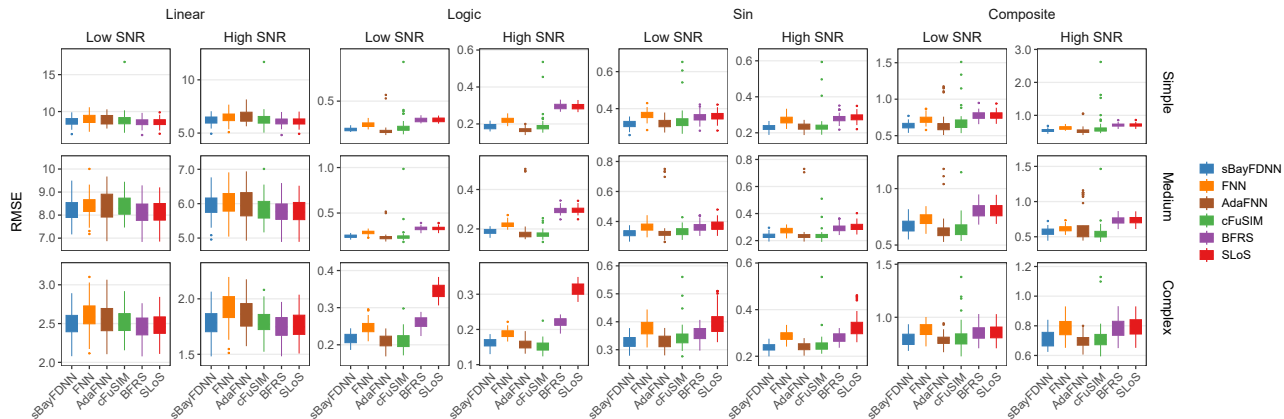

 Figure 4. RMSE across g functions, SNR settings, and $\beta(t)$ scenarios.

Table 1. Performance on ECG and Tecator datasets. F1, Recall, and Precision are reported only for methods that output an estimated active region; otherwise shown as “–”. Best results within each dataset/metric are in bold.

Method	ECG					Tecator				
	RMSE	MAE	F1	Recall	Precision	RMSE	MAE	F1	Recall	Precision
sBayFDNN	12.069	8.711	0.634	1.000	0.464	2.138	1.594	0.339	1.000	0.204
FNN	12.991	9.239	–	–	–	2.217	1.613	–	–	–
AdaFNN	14.083	10.198	–	–	–	3.027	2.299	–	–	–
cFuSIM	17.677	12.861	0.501	1.000	0.334	3.932	3.283	0.137	0.977	0.074
BFRS	16.297	11.805	0.396	0.784	0.265	2.691	2.250	0.211	0.714	0.124
SLoS	16.258	11.782	0.412	0.815	0.276	2.567	2.068	0.228	0.854	0.132

Table 2. Performance on Bike rental and IHPC datasets.

Method	Bike		IHPC	
	RMSE	MAE	RMSE	MAE
sBayFDNN	0.618	0.497	0.536	0.409
FNN	0.699	0.535	0.549	0.409
AdaFNN	0.720	0.577	0.552	0.420
cFuSIM	0.693	0.539	0.548	0.411
BFRS	0.749	0.550	0.552	0.416
SLoS	0.684	0.506	0.549	0.411

7. Conclusion

We have presented a sparse Bayesian functional DNN framework that performs automatic region selection for nonlinear scalar-on-function regression. By integrating B-spline expansions with a Bayesian neural network and imposing a structured spike-and-slab prior, our model captures complex nonlinear dependencies between functional predictors and scalar responses through data-driven functional representations and a flexible deep architecture. The framework provides interpretable region-wise selection and principled uncertainty quantification, supported by theoretical guarantees. Simulations and experiments on multiple real-world datasets confirm its selection accuracy and competitive predictive performance, demonstrating practical utility in identifying region-specific functional effects.

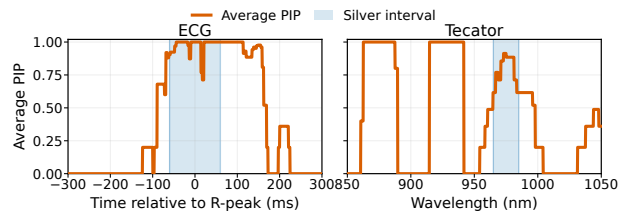


Figure 5. PIPs from sBayFDNN for ECG and Tecator datasets.

Future work includes extending the framework to jointly model functional and discrete covariates, rather than pre-adjusting for confounders. The approach can also be generalized to handle multiple functional predictors with simultaneous variable and region selection. Replacing the l_2 loss with a more robust alternative may improve stability in noisy settings, while embedding the model within a generalized linear model would allow applications to binary, count, or survival outcomes, further broadening its utility in functional data analysis.

Software and Data

The implementation code for sBayFDNN is available in the Supplementary Material, while the download link for the accompanying real dataset is provided in the Appendix.

Impact Statement

This work introduces a Bayesian deep learning framework for interpretable region selection in functional data. It advances nonlinear function-to-scalar regression by integrating structured sparsity with principled uncertainty quantification. The primary aim is to enhance machine learning methodology for functional and structured data. The proposed framework benefits domains where interpretability and reliability are essential, such as spectral chemometrics, neural signal analysis, and clinical monitoring. By enabling precise identification of informative functional subdomains, the method can support more accurate material composition analysis, refined physiological signal interpretation, and more targeted diagnostic interventions.

References

- Atashgahi, Z., Zhang, X., Kichler, N., Liu, S., Yin, L., Pechenizkiy, M., Veldhuis, R., and Mocanu, D. C. Supervised feature selection with neuron evolution in sparse neural networks. *Transactions on Machine Learning Research*, 2023. ISSN 2835-8856. URL <https://openreview.net/forum?id=GcO6ugrLKp>. Featured Certification.
- Belli, E. Smoothly adaptively centered ridge estimator. *Journal of Multivariate Analysis*, 189:104882, 2022.
- Cai, T. T. and Yuan, M. Minimax and adaptive prediction for functional linear regression. *Journal of the American Statistical Association*, 107(499):1201–1216, 2012.
- Cardot, H., Ferraty, F., and Sarda, P. Spline estimators for the functional linear model. *Statistica Sinica*, pp. 571–591, 2003.
- Chen, Y., Gao, Q., Liang, F., and Wang, X. Nonlinear variable selection via deep neural networks. *Journal of Computational and Graphical Statistics*, 30(2):484–492, 2021.
- Chu, Z., Claridy, M., Cordero, J., Li, S., and Rathbun, S. L. Estimating propensity scores with deep adaptive variable selection. In *Proceedings of the 2023 SIAM International Conference on Data Mining (SDM)*, pp. 730–738. SIAM, 2023.
- Crambes, C., Kneip, A., and Sarda, P. Smoothing splines estimators for functional linear regression. *The Annals of Statistics*, 37(1):35–72, 2009.
- Dinh, V. C. and Ho, L. S. Consistent feature selection for analytic deep neural networks. *Advances in Neural Information Processing Systems*, 33:2420–2431, 2020.
- Elias, P. and Finer, J. EchoNext: A Dataset for Detecting Echocardiogram-Confirmed Structural Heart Disease from ECGs. *PhysioNet*, September 2025. doi: 10.13026/3ykd-bf14. URL <https://doi.org/10.13026/3ykd-bf14>. Version 1.1.0.
- Fan, J., Yang, J., Ma, S., and Wu, M. Bilevel network learning via hierarchically structured sparsity. In *The Thirty-ninth Annual Conference on Neural Information Processing Systems*, 2025.
- Fan, Y. and Waldmann, P. Multi-task genomic prediction using gated residual variable selection neural networks. *BMC Bioinformatics*, 26(1):167, 2025.
- Fanaee-T, H. Bike Sharing. UCI Machine Learning Repository, 2013. DOI: <https://doi.org/10.24432/C5W894>.
- Ghosal, S., Ghosh, J. K., and Van Der Vaart, A. W. Convergence rates of posterior distributions. *The Annals of Statistics*, 28(2):500–531, 2000.
- Goldberger, A. L., Amaral, L. A., Glass, L., Hausdorff, J. M., Ivanov, P. C., Mark, R. G., Mietus, J. E., Moody, G. B., Peng, C.-K., and Stanley, H. E. Physiobank, physiotoolkit, and physionet: components of a new research resource for complex physiologic signals. *Circulation*, 101(23):e215–e220, 2000.
- Hebrail, G. and Berard, A. Individual Household Electric Power Consumption. UCI Machine Learning Repository, 2006. DOI: <https://doi.org/10.24432/C58K54>.
- Hummel, S. L., Skorcz, S., and Koelling, T. M. Prolonged electrocardiogram qrs duration independently predicts long-term mortality in patients hospitalized for heart failure with preserved systolic function. *Journal of Cardiac Failure*, 15(7):553–560, 2009.
- Jiang, F., Baek, S., Cao, J., and Ma, Y. A functional single-index model. *Statistica sinica*, 30(1):303–324, 2020.
- Jiang, W. Bayesian variable selection for high dimensional generalized linear models: Convergence rates of the fitted densities. *The Annals of Statistics*, 35(4):1487–1511, 2007.
- Kachuee, M., Fazeli, S., and Sarrafzadeh, M. Ecg heart-beat classification: A deep transferable representation. In *2018 IEEE International Conference on Healthcare Informatics (ICHI)*, pp. 443–444. IEEE, 2018.
- Kashani, A. and Barold, S. S. Significance of qrs complex duration in patients with heart failure. *Journal of the American College of Cardiology*, 46(12):2183–2192, 2005.

- Lee, E. R. and Park, B. U. Sparse estimation in functional linear regression. *Journal of Multivariate Analysis*, 105(1):1–17, 2012.
- Lemhadri, I., Ruan, F., Abraham, L., and Tibshirani, R. Lassonet: A neural network with feature sparsity. *Journal of Machine Learning Research*, 22(127):1–29, 2021.
- Lin, Z., Cao, J., Wang, L., and Wang, H. Locally sparse estimator for functional linear regression models. *Journal of Computational and Graphical Statistics*, 26(2):306–318, 2017.
- Luo, B. and Halabi, S. Sparse-input neural network using group concave regularization. *Transactions on Machine Learning Research*, 2025. ISSN 2835-8856. URL <https://openreview.net/forum?id=m9UsLHZYeX>. Featured Certification.
- Makowski, D., Pham, T., Lau, Z. J., Brammer, J. C., Lespinasse, F., Pham, H., Schölzel, C., and Chen, S. A. Neurokit2: A python toolbox for neurophysiological signal processing. *Behavior Research Methods*, 53(4):1689–1696, 2021.
- Moor, M., Banerjee, O., Abad, Z. S. H., Krumholz, H. M., Leskovec, J., Topol, E. J., and Rajpurkar, P. Foundation models for generalist medical artificial intelligence. *Nature*, 616(7956):259–265, 2023.
- Nie, Y., Wang, L., and Cao, J. Estimating functional single index models with compact support. *Environmetrics*, 34(2):e2784, 2023.
- Pang, J. C., Aquino, K. M., Oldehinkel, M., Robinson, P. A., Fulcher, B. D., Breakspear, M., and Fornito, A. Geometric constraints on human brain function. *Nature*, 618(7965):566–574, 2023.
- Sun, Y., Song, Q., and Liang, F. Consistent sparse deep learning: Theory and computation. *Journal of the American Statistical Association*, 117(540):1981–1995, 2022.
- Thind, B., Multani, K., and Cao, J. Deep learning with functional inputs. *Journal of Computational and Graphical Statistics*, 32(1):171–180, 2023.
- Thodberg, H. H. Tecator meat sample dataset. StatLib Datasets Archive, 2015. <http://lib.stat.cmu.edu/datasets/tecator>.
- Tsai, K., Zhao, B., Koyejo, S., and Kolar, M. Latent multimodal functional graphical model estimation. *Journal of the American Statistical Association*, 119(547):2217–2229, 2024.
- van Kollenburg, G. H., van Manen, H.-J., Admiraal, N., Gerretzen, J., and Jansen, J. J. Low-cost handheld nir spectroscopy for identification of organic solvents and low-level quantification of water contamination. *Talanta*, 223:121865, 2021.
- Wang, S., Cao, G., Shang, Z., and Initiative, A. D. N. Deep neural network classifier for multidimensional functional data. *Scandinavian Journal of Statistics*, 50(4):1667–1686, 2023.
- Wu, S., Beaulac, C., and Cao, J. Functional autoencoder for smoothing and representation learning. *Statistics and Computing*, 34(6):203, 2024.
- Yang, J., Li, T., Wang, T., Ma, S., and Wu, M. Heterogeneous gene network estimation for single-cell transcriptomic data via a joint regularized deep neural network. *Journal of the American Statistical Association*, (just-accepted):1–16, 2026.
- Yao, J., Mueller, J., and Wang, J.-L. Deep learning for functional data analysis with adaptive basis layers. In *International Conference on Machine Learning*, pp. 11898–11908. PMLR, 2021.
- Yarotsky, D. Optimal approximation of continuous functions by very deep relu networks. In *Conference on Learning Theory*, pp. 639–649. PMLR, 2018.
- Yu, C., Lin, H., Zhang, Q., and Sanderson, J. High prevalence of left ventricular systolic and diastolic asynchrony in patients with congestive heart failure and normal qrs duration. *Heart*, 89(1):54–60, 2003.
- Zhu, H., Sun, Y., and Lee, J. Bayesian functional region selection. *Stat*, 14(1):e70047, 2025.
- Zubkov, A. M. and Serov, A. A. A complete proof of universal inequalities for the distribution function of the binomial law. *Theory of Probability & Its Applications*, 57(3):539–544, 2013.

A. Details for the posterior inference

A.1. Hyperparameter settings

All responses Y are standardized using training-set statistics; unless otherwise stated, all computations are carried out on this standardized scale and we set the noise variance to $\sigma_\varepsilon^2 = 1$. For non-sparsified network parameters, we use independent Gaussian priors with variance $\sigma^2 = 1$ (numerically equal to σ_ε^2 under standardization, but conceptually distinct). We use $R = 5$ random restarts for each J_n .

Simulation defaults.

- Basis: B-splines with degree 4 (unless otherwise stated).
- Network: fully-connected ReLU, 64–64–64–1; first-layer column-wise spike-and-slab selection.
- Optimizer: mini-batch SGD, learning rate 10^{-3} , batch size 64, max 80,001 iterations, early stopping patience 3,000.
- Spike-and-slab: $(\lambda_n, \sigma_{0,n}^2, \sigma_{1,n}^2) = (10^{-5}, 10^{-5}, 2 \times 10^{-3})$.

We treat the projection truncation level J_n as a resolution hyperparameter and select it via restart-aggregated evidence in simulations or restart-aggregated validation loss when evidence computation is prohibitive. We use the candidate set $\mathcal{J} = \{55, 60, 70, 80\}$ for J_n in simulations; for real datasets, \mathcal{J} is chosen as a small neighborhood around a dataset-specific baseline resolution.

We train with a small learning rate and a relatively large early-stopping patience to obtain stable solutions across restarts. The sparsification prior is intentionally strong in simulations; empirically, the same default sparsification hyperparameters remain effective on ECG ($n \approx 2-3 \times 10^4$), consistent with increasingly data-dominated inference as n grows.

For competing methods, we aim to ensure fair comparisons by using comparable model capacity whenever applicable (e.g., similar depth/width for neural-network baselines). Method-specific hyperparameters are taken from authors' recommended defaults when available, and otherwise selected by cross-validation or validation loss on the same training/validation split.

A.2. Stochastic gradient algorithm (SGD) for the MAP fitting

We first provide the derivations on the marginal prior on θ . Denote $K_{1_n} = (J_n + 1)L_1 + \sum_{k=2}^{H_n} (L_{k-1} + 1)L_k$ as the dimension of θ and $\mathcal{W} \subset \{1, \dots, K_{1_n}\}$ as the set of indices in θ corresponding to the weights of the first-layer $\{W_{1,hg}\}_{h \leq L_1, g \leq J_n}$, and let $\mathcal{G} := \{1, \dots, K_{1_n}\} \setminus \mathcal{W}$. In addition, let $\phi(\cdot; 0, s^2)$ denote the $\mathcal{N}(0, s^2)$ density.

Based on the priors introduced in Section 3, we have

$$\begin{aligned} \pi(\mathbf{W}_{1,*j} \mid \gamma_j) &= \prod_{h=1}^{L_1} \left[\phi(W_{1,hj}; 0, \sigma_{1,n}^2) \right]^{\gamma_j} \left[\phi(W_{1,hj}; 0, \sigma_{0,n}^2) \right]^{1-\gamma_j}, \forall j \in \{1, \dots, J_n\}; \\ \pi(\gamma_j) &= \lambda_n^{\gamma_j} (1 - \lambda_n)^{1-\gamma_j}; \\ \pi(W_{h,ab}) &= \phi(W_{h,ab}; 0, \sigma^2), \quad \forall h \in \{2, \dots, H_n\}; \\ &\text{and} \\ \pi(b_{h,a}) &= \phi(b_{h,a}; 0, \sigma^2), \quad \forall h \in \{1, \dots, H_n\}. \end{aligned}$$

Then, the marginal prior on θ is $\pi(\theta) = \sum_{\gamma} \pi(\theta, \gamma)$, where

$$\pi(\theta, \gamma) = \prod_{j=1}^{J_n} [\pi(\gamma_j) \pi(\mathbf{W}_{1,*j} \mid \gamma_j)] \prod_{j \in \mathcal{G}} \phi(\theta_j; 0, \sigma^2).$$

Based on the marginal prior on θ , we develop the following SGD algorithm (Algorithm 1) for optimizing (9).

After selecting J^* , we form the final predictor by averaging the outputs of the R independently trained models at J^* , i.e., $\hat{y}(x) = R^{-1} \sum_{r=1}^R f_{\hat{\theta}_{J^*,r}}(\eta_{J^*}(x))$. For interpretability metrics (e.g., feature masks/PIP), we report results from the single restart r^* with the smallest validation loss.

In Step 5 of Algorithm 1, we score each run by the Bayesian evidence using a Laplace approximation (see, e.g., MacKay, 1992; Liang et al., 2005). Let $\mathcal{L}_{n,J}(\boldsymbol{\theta})$ denote the (negative) log-posterior objective used in MAP training under projection dimension J , and define $h_{n,J}(\boldsymbol{\theta}) := -\mathcal{L}_{n,J}(\boldsymbol{\theta})/n_{\text{tr}}$. Let $\mathbf{H}_{n,J}(\boldsymbol{\theta}) := \nabla_{\boldsymbol{\theta}}^2 h_{n,J}(\boldsymbol{\theta})$. For evidence computation we evaluate $h_{n,J}$ and $\mathbf{H}_{n,J}$ at the sparsified surrogate parameter $\widehat{\boldsymbol{\theta}}_{J,r}^s$ (constructed in Step 4), while predictive evaluations are based on the MAP estimate $\widehat{\boldsymbol{\theta}}_{J,r}$.

Let $\mathcal{I}_{J,r}$ index the parameters retained for evidence computation (i.e., the free parameters under the sparsified surrogate), and let $d_{J,r} := |\mathcal{I}_{J,r}|$. Denote by $\mathbf{H}_{n,J}(\boldsymbol{\theta})_{\mathcal{I}_{J,r},\mathcal{I}_{J,r}}$ the corresponding principal submatrix. The Laplace-approximated log-evidence is

$$\ell_{J,r} := n_{\text{tr}} h_{n,J}(\widehat{\boldsymbol{\theta}}_{J,r}^s) + \frac{d_{J,r}}{2} \log(2\pi) - \frac{d_{J,r}}{2} \log(n_{\text{tr}}) - \frac{1}{2} \log \det \left(-\mathbf{H}_{n,J}(\widehat{\boldsymbol{\theta}}_{J,r}^s)_{\mathcal{I}_{J,r},\mathcal{I}_{J,r}} \right), \quad (10)$$

where $-\mathbf{H}_{n,J}(\widehat{\boldsymbol{\theta}}_{J,r}^s)_{\mathcal{I}_{J,r},\mathcal{I}_{J,r}}$ is the negative Hessian at the mode restricted to the retained parameters.

We compute the log-determinant term in (10) via eigenvalues of the restricted Hessian for numerical stability, and apply standard stabilization when needed (e.g., adding a small diagonal jitter).

B. Proof of Statistical Properties

We divide the theoretical proof into four parts. First, we establish the theoretical foundation for finite-dimensional approximations of functional data, which lays the groundwork for the subsequent theorems. Then, in the second, third, and fourth parts, we provide proofs for the bound of the approximation error (Theorem 5.4), the posterior consistency (Theorem 5.7), and the selection consistency (Theorem 5.9), respectively. Prior to proving each theorem, we present necessary lemmas. Throughout, C, C', C_1, \dots denote generic positive constants whose values may change from line to line.

B.1. Finite-dimensional approximations

First, recall and introduce some notations. Let β^* and $\beta_{J_n}^* = \sum_{j=1}^{J_n} \omega_{J_n,j}^* B_j(t)$ denote the true coefficient function and its truncated counterpart, respectively, where $\boldsymbol{\omega}_{J_n}^* = (\omega_{J_n,1}^*, \dots, \omega_{J_n,J_n}^*)^T$ is the vector of true basis coefficients for $\beta_{J_n}^*$. Denote $S_{J_n}^* = \text{supp}(\boldsymbol{\omega}_{J_n}^*)$ and $\Omega_{J_n}^* = \cup_{j \in S_{J_n}^*} I_j$ with $I_j := \text{supp}(B_j)$. In addition, let $u^*(X) := \langle X, \beta^* \rangle$, $\mu^*(X) := g^*(u^*(X))$, $u_{J_n}^*(X) := \langle X, \beta_{J_n}^* \rangle$, and $\mu_{J_n}^*(X) := g^*(u_{J_n}^*(X))$. Moreover, for $\kappa > 0$, define the strong-signal region $\Omega^*(\kappa) := \{t \in [0, 1] : |\beta^*(t)| > \kappa\}$. Define $S_{J_n}^*(\kappa) := \{j \in [J_n] : I_j \cap \Omega^*(\kappa) \neq \emptyset\}$ and $\Omega_{J_n}^*(\kappa) := \cup_{j \in S_{J_n}^*(\kappa)} I_j$. Let $\Delta_{J_n} := \max_{1 \leq j \leq J_n} \text{diam}(I_j) \asymp J_n^{-1}$ for fixed spline order. For a measurable set $A \subset [0, 1]$ and $\Delta > 0$, define its Δ -enlargement by $A^{+\Delta} := \{t \in [0, 1] : \text{dist}(t, A) \leq \Delta\}$. For the strong-signal cover $\Omega_{J_n}^*(\kappa)$, we will also use the enlarged cover $\Omega_{J_n}^*(\kappa)^{+c_{\text{loc}}\Delta_{J_n}}$, where $c_{\text{loc}} \geq 1$ is an absolute constant depending only on the locality radius of the spline quasi-interpolant/projection used below.

Lemma B.1. *Suppose Assumption 5.1–5.3 holds. Define $\kappa_{J_n} := c_{\kappa} C_{\beta} J_n^{-\alpha_{\beta}}$ with $c_{\kappa} \geq 4$ and C_{β} being some constant. Then for all sufficiently large n , we have*

(i) *Uniform approximation at resolution J_n :*

$$\|\beta^* - \beta_{J_n}^*\|_{\infty} \leq C J_n^{-\alpha_{\beta}} \lesssim \kappa_{J_n}. \quad (11)$$

Moreover, on the strong-signal set $\Omega^(2\kappa_{J_n})$:*

$$\|\beta^* - \beta_{J_n}^*\|_{L^{\infty}(\Omega^*(2\kappa_{J_n}))} \leq C_{\beta} J_n^{-\alpha_{\beta}} \leq \kappa_{J_n}/c_{\kappa}, \quad (12)$$

where $\|v(t)\|_{L^{\infty}(\Omega^(2\kappa_{J_n}))} = \sup_{t \in \Omega^*(2\kappa_{J_n})} |v(t)|$.*

(ii) *Localization to the strong-signal cover: There exists an absolute constant $c_{\text{loc}} \geq 1$ and $\Delta_{J_n} \asymp J_n^{-1}$ such that, for all sufficiently large n ,*

$$\Omega_{J_n}^* \subseteq \Omega_{J_n}^*(\kappa_{J_n})^{+c_{\text{loc}}\Delta_{J_n}}. \quad (13)$$

(iii) *Index and link truncation: letting $\alpha_1 = \min(\alpha_g, 1)$,*

$$\sup_{X \in \mathcal{X}} |u_{J_n}^*(X) - u^*(X)| \leq C_X \|\beta_{J_n}^* - \beta^*\|_{\infty} \lesssim J_n^{-\alpha_{\beta}}, \quad (14)$$

and

$$\sup_{X \in \mathcal{X}} |\mu_{J_n}^*(X) - \mu^*(X)| = \sup_{X \in \mathcal{X}} |g^*(u_{J_n}^*(X)) - g^*(u^*(X))| \leq L_g \left(\sup_{X \in \mathcal{X}} |u_{J_n}^*(X) - u^*(X)| \right)^{\alpha_1} \lesssim J_n^{-\alpha_\beta \alpha_1}. \quad (15)$$

(iv) *Strong-signal sandwich:*

$$\Omega^*(2\kappa_{J_n}) \subseteq \Omega_{J_n}^* \subseteq \Omega_{J_n}^*(\kappa_{J_n})^{+c_{\text{loc}}\Delta_{J_n}}. \quad (16)$$

(v) *Gap decomposition (no extra structure assumed):*

$$|\Omega_{J_n}^* \Delta \Omega^*(2\kappa_{J_n})| \leq \underbrace{|\Omega^*(\kappa_{J_n}) \setminus \Omega^*(2\kappa_{J_n})|}_{\text{threshold band}} + \underbrace{|\Omega_{J_n}^*(\kappa_{J_n})^{+c_{\text{loc}}\Delta_{J_n}} \setminus \Omega^*(\kappa_{J_n})|}_{\text{resolution boundary layer}}. \quad (17)$$

Proof. Step 1 (spline approximation and the choice of Q_{J_n}). Fix a local B-spline basis $\{B_j\}_{j=1}^{J_n}$ of fixed order on $[0, 1]$ with supports I_j and $\Delta_{J_n} := \max_{1 \leq j \leq J_n} \text{diam}(I_j) \asymp J_n^{-1}$. Let Q_{J_n} denote a *local* spline quasi-interpolant/projection onto the corresponding spline space (e.g., a standard quasi-interpolant associated with the B-spline partition). By standard L_∞ spline approximation theory, for any $\beta \in \mathcal{H}^{\alpha_\beta}([0, 1])$,

$$\|\beta - Q_{J_n}\beta\|_\infty \leq C_\beta J_n^{-\alpha_\beta}.$$

In the sequel, we work with this fixed operator Q_{J_n} .

Step 2 (localization with an enlarged cover). Recall $\kappa_{J_n} = c_\kappa C_\beta J_n^{-\alpha_\beta}$. Construct a smooth cut-off function $\chi_{J_n} : [0, 1] \rightarrow [0, 1]$ such that

$$\chi_{J_n}(t) = 1 \text{ for } t \in \Omega^*(2\kappa_{J_n}), \quad \chi_{J_n}(t) = 0 \text{ for } t \in \Omega^*(\kappa_{J_n})^c,$$

and on the transition band $\Omega^*(\kappa_{J_n}) \cap \Omega^*(2\kappa_{J_n})^c$, one has $0 < \chi_{J_n}(t) < 1$ (with χ_{J_n} chosen smooth across the boundaries of these sets). Define the truncated coefficient

$$\beta^{\text{loc}}(t) := \beta^*(t)\chi_{J_n}(t).$$

Then $\text{supp}(\beta^{\text{loc}}) \subseteq \Omega^*(\kappa_{J_n})$ and, since $1 - \chi_{J_n}$ vanishes on $\Omega^*(2\kappa_{J_n})$ and is supported inside $\Omega^*(\kappa_{J_n})^c \cup (\Omega^*(\kappa_{J_n}) \cap \Omega^*(2\kappa_{J_n})^c)$,

$$\|\beta^* - \beta^{\text{loc}}\|_\infty = \sup_{t \in [0, 1]} |\beta^*(t)\{1 - \chi_{J_n}(t)\}| \leq \sup_{t \in \Omega^*(\kappa_{J_n})^c} |\beta^*(t)| \leq 2\kappa_{J_n}.$$

Moreover, $\beta^{\text{loc}} \in \mathcal{H}^{\alpha_\beta}([0, 1])$ with the same smoothness order, since $\beta^* \in \mathcal{H}^{\alpha_\beta}$ and χ_{J_n} is smooth and bounded.

Now define

$$\beta_{J_n}^* := Q_{J_n}\beta^{\text{loc}}.$$

By the locality of Q_{J_n} , there exists an absolute constant $c_{\text{loc}} \geq 1$ such that

$$\text{supp}(Q_{J_n}f) \subseteq \text{supp}(f)^{+c_{\text{loc}}\Delta_{J_n}} \quad \text{for all bounded } f.$$

Therefore,

$$\text{supp}(\beta_{J_n}^*) \subseteq \text{supp}(\beta^{\text{loc}})^{+c_{\text{loc}}\Delta_{J_n}} \subseteq \Omega^*(\kappa_{J_n})^{+c_{\text{loc}}\Delta_{J_n}} \subseteq \Omega_{J_n}^*(\kappa_{J_n})^{+c_{\text{loc}}\Delta_{J_n}},$$

where the last inclusion uses $\Omega^*(\kappa_{J_n}) \subseteq \Omega_{J_n}^*(\kappa_{J_n})$. Since $\Omega_{J_n}^* = \text{supp}(\beta_{J_n}^*)$ by local linear independence of the B-spline basis, we obtain $\Omega_{J_n}^* \subseteq \Omega_{J_n}^*(\kappa_{J_n})^{+c_{\text{loc}}\Delta_{J_n}}$, which proves (13).

For approximation, note that on $\Omega^*(2\kappa_{J_n})$, we have $\beta^{\text{loc}} = \beta^*$, hence

$$\|\beta^* - \beta_{J_n}^*\|_{L^\infty(\Omega^*(2\kappa_{J_n}))} = \|\beta^{\text{loc}} - Q_{J_n}\beta^{\text{loc}}\|_{L^\infty(\Omega^*(2\kappa_{J_n}))} \leq \|\beta^{\text{loc}} - Q_{J_n}\beta^{\text{loc}}\|_\infty \leq C_\beta J_n^{-\alpha_\beta},$$

which gives (12). Globally,

$$\|\beta^* - \beta_{J_n}^*\|_\infty \leq \|\beta^* - \beta^{\text{loc}}\|_\infty + \|\beta^{\text{loc}} - Q_{J_n}\beta^{\text{loc}}\|_\infty \leq 2\kappa_{J_n} + C_\beta J_n^{-\alpha_\beta} \lesssim J_n^{-\alpha_\beta}.$$

This proves (11).

Step 3 (index and link truncation). By Assumption 5.1,

$$|u_{J_n}^*(X) - u^*(X)| = \left| \int_0^1 X(t)(\beta_{J_n}^*(t) - \beta^*(t)) dt \right| \leq \|X\|_{L^1} \|\beta_{J_n}^* - \beta^*\|_\infty \leq C_X \|\beta_{J_n}^* - \beta^*\|_\infty,$$

and (14) follows from (11). The link bound (15) follows from Hölder continuity of g^* .

Step 4 (sandwich). Take $t \in \Omega^*(2\kappa_{J_n})$. Then $|\beta^*(t)| > 2\kappa_{J_n}$ and by (12),

$$|\beta_{J_n}^*(t)| \geq |\beta^*(t)| - \|\beta^* - \beta_{J_n}^*\|_{L^\infty(\Omega^*(2\kappa_{J_n}))} > 2\kappa_{J_n} - \kappa_{J_n}/c_\kappa > 0$$

since $c_\kappa \geq 4$. Hence $t \in \text{supp}(\beta_{J_n}^*)$. For standard local B-spline bases (local linear independence), $\text{supp}(\beta_{J_n}^*) = \cup_{j \in S_{J_n}^*} I_j = \Omega_{J_n}^*$, so $\Omega^*(2\kappa_{J_n}) \subseteq \Omega_{J_n}^*$. The right inclusion $\Omega_{J_n}^* \subseteq \Omega_{J_n}^*(\kappa_{J_n})^{+c_{\text{loc}}\Delta_{J_n}}$ follows from (13). This proves (16).

Step 5 (gap decomposition). By (16),

$$\Omega_{J_n}^* \Delta \Omega^*(2\kappa_{J_n}) \subseteq \Omega_{J_n}^*(\kappa_{J_n})^{+c_{\text{loc}}\Delta_{J_n}} \setminus \Omega^*(2\kappa_{J_n}) = (\Omega^*(\kappa_{J_n}) \setminus \Omega^*(2\kappa_{J_n})) \cup (\Omega_{J_n}^*(\kappa_{J_n})^{+c_{\text{loc}}\Delta_{J_n}} \setminus \Omega^*(\kappa_{J_n})),$$

and (17) follows by subadditivity of Lebesgue measure. \square

B.2. Approximation error bounds (Theorem 5.4)

Lemma B.2. *Suppose Assumption 5.6 holds such that there exists L_g satisfy $|g^*(u) - g^*(v)| \leq L_g|u - v|^{\alpha_1}$ for all $u, v \in [0, 1]$ with $\alpha_1 = \min(\alpha_g, 1)$. Then for any integer depth $H_n \geq 2$, there exists a univariate ReLU network f_{H_n} with constant width (at most a universal constant) and depth at most H_n such that*

$$\sup_{u \in [0, 1]} |f_{H_n}(u) - g^*(u)| \lesssim H_n^{-2\alpha_1}.$$

Proof. This result is a direct specialization of Theorem 2 in Yarotsky (2018) to the one-dimensional setting. Taking input dimension $d = 1$ and approximation accuracy $\varepsilon \asymp H_n^{-2\alpha_1}$ in that theorem yields the stated rate with constant network width. \square

B.2.1. PROOF OF THEOREM 5.4

The proof is structured into three steps. First, for the unknown link function $g^*(u)$, Lemma B.2 guarantees the existence of a one-dimensional neural network f_{H_n-1} with constant width and depth $H_n - 1$ such that

$$\sup_{u \in [0, 1]} |f_{H_n-1}(u) - g^*(u)| \lesssim H_n^{-2\alpha_1}.$$

Furthermore, the network output $f_{H_n-1}(u_{J_n}^*(X))$, where $u_{J_n}^*(X) = (\omega_{J_n}^*)^\top \boldsymbol{\eta}(X)$, can be reinterpreted as an H_n -depth network F_θ with J_n -dimensional input $\boldsymbol{\eta}(X)$. To construct F_θ , we explicitly design its first hidden layer to satisfy the support condition $\text{supp}_{\text{col}}(\boldsymbol{\theta}) = S_{J_n}^*$: we set the width of the first layer as $L_1 \asymp 1$, the weights of the first neuron in the first hidden layer to be $\mathbf{W}_{1,1*} = (\omega_{J_n}^*)^\top$ and all other row weights $\mathbf{W}_{1,j*} = \mathbf{0}^\top$ for $j > 1$. The remaining layers then implement f_{H_n-1} acting on the computed scalar $(\omega_{J_n}^*)^\top \boldsymbol{\eta}(X)$. This yields a DNN F_θ with depth at most H_n , constant width up to universal constants, and $\text{supp}_{\text{col}}(\boldsymbol{\theta}) = S_{J_n}^*$, establishing (i).

Finally, to prove (ii), we decompose the approximation error into a network approximation error and a functional truncation error. For any $X \in \mathcal{X}$,

$$\begin{aligned} |\mu_\theta(X) - \mu^*(X)| &= |F_\theta(\boldsymbol{\eta}(X)) - g^*(u^*(X))| \\ &= |f_{H_n-1}(u_{J_n}^*(X)) - g^*(u^*(X))| \\ &\leq \underbrace{|f_{H_n-1}(u_{J_n}^*(X)) - g^*(u_{J_n}^*(X))|}_I + \underbrace{|g^*(u_{J_n}^*(X)) - g^*(u^*(X))|}_{II}. \end{aligned}$$

Term I is bounded directly by Lemma B.2, while term II is controlled via inequality (15) from Lemma B.1. Taking the supremum over \mathcal{X} then yields the final convergence rate stated in (ii).

B.3. Posterior consistency (Theorem 5.7)

We first give a general posterior consistency result introduced in Jiang (2007). Specifically, let $D_n = \{(\mathbf{x}_i, Y_i)\}_{i=1}^n$ denote the dataset, where (\mathbf{x}_i, Y_i) are i.i.d. under the reference distribution p^* . Let \mathcal{P} denote the space of probability densities under consideration. We consider a sequence of model classes (sieves) $P_n \subset \mathcal{P}$, and write $P_n^c = \mathcal{P} \setminus P_n$ for their complements. We construct P_n through a parameter sieve Θ_n via

$$P_n := \{p_\theta : \theta \in \Theta_n\}.$$

Let Π denote the prior measure on \mathcal{P} (or on Θ via p_θ), and let $\Pi(\cdot | D_n)$ denote the corresponding posterior given the data D_n . For each $\varepsilon > 0$, define the posterior probability

$$\widehat{\Pi}(\varepsilon) := \Pi(d(p, p^*) > \varepsilon | D_n),$$

where the metric $d(\cdot, \cdot)$ denotes the Hellinger distance, defined by $d(p, q) = \sqrt{\int (\sqrt{p} - \sqrt{q})^2}$. Let $N(\varepsilon, P_n, d)$ denote the ε -covering number of P_n with respect to the metric d .

Lemma B.3. *For a sequence $\varepsilon_n \rightarrow 0$, if there exist constants $2 > b > 2b' > 0$ and $t > 0$ such that the following conditions hold for all sufficiently large n :*

- (a) $\log N(\varepsilon_n, P_n, d) \leq n\varepsilon_n^2$;
- (b) $\pi(P_n^c) \leq \exp(-bn\varepsilon_n^2)$;
- (c) $\pi\{p \in \mathcal{P} : d_t(p, p^*) \leq b'\varepsilon_n^2\} \geq \exp(-b'n\varepsilon_n^2)$,

where $d_t(p, p^*) = \frac{1}{t} \left(\int p^*(x) \left(\frac{p^*(x)}{p(x)} \right)^t dx - 1 \right)$, then for any $2b' < x < b$, the posterior probability $\widehat{\Pi}(4\varepsilon_n)$ satisfies:

- (i) $P \left[\widehat{\Pi}(4\varepsilon_n) \geq 2 \exp \left(-\frac{1}{2} n\varepsilon_n^2 m(x) \right) \right] \leq 2 \exp \left(-\frac{1}{2} n\varepsilon_n^2 m(x) \right)$,
- (ii) $\mathbb{E} \left[\widehat{\Pi}(4\varepsilon_n) \right] \leq 4 \exp \left(-n\varepsilon_n^2 m(x) \right)$,

where $m(x) := \min\{1, 2 - x, b - x, t(x - 2b')\}$.

Proof. The proof follows from an argument analogous to that of Proposition 1 in Jiang (2007). □

Lemma B.4. *Fix any subset $S \subset \{1, \dots, J_n\}$ with $m := |S|$. Consider the proposed DNN F_θ defined in (4) with input of dimension J_n . Let θ be a network parameter vector with $\|\theta\|_\infty \leq E_n$. Let $\tilde{\theta}$ be another parameter vector such that*

$$|W_{1,hg} - \tilde{W}_{1,hg}| \leq \begin{cases} \delta_1, & g \in S, \\ \delta_2, & g \notin S, \end{cases} \quad 1 \leq h \leq L_1, 1 \leq g \leq J_n,$$

and for all deeper-layer coordinates \mathcal{G} , including all biases and weights beyond the first layer,

$$\max_{j \in \mathcal{G}} |\theta_j - \tilde{\theta}_j| \leq \delta_1.$$

Then, for all $\mathbf{x} \in [-1, 1]^{J_n}$,

$$\begin{aligned} |F_\theta(\mathbf{x}) - F_{\tilde{\theta}}(\mathbf{x})| &\leq (E_n + \delta_1)^{H_n - 1} \left[H_n (m + 1) L_1 \prod_{k=2}^{H_n} (L_{k-1} + 1) L_k \delta_1 \right. \\ &\quad \left. + \left\{ (J_n - m) L_1 \prod_{k=2}^{H_n} (L_{k-1} + 1) L_k \right\} \delta_2 \right]. \end{aligned}$$

Proof. Consider the pre-activation at the first layer $z_{1,h} = \sum_{g=1}^{J_n} W_{1,hg}x_g + b_{1,h}$. For any $\mathbf{x} \in [-1, 1]^{J_n}$, the difference satisfies:

$$|z_{1,h} - \tilde{z}_{1,h}| \leq \sum_{g \in S} \delta_1 |x_g| + \sum_{g \notin S} \delta_2 |x_g| + \delta_1 \leq (m+1)\delta_1 + (J_n - m)\delta_2.$$

For $k \geq 2$, let \mathbf{z}_k denote the pre-activation vector of layer k . Since ReLU is 1-Lipschitz, the error propagates as:

$$\|\mathbf{z}_k - \tilde{\mathbf{z}}_k\|_\infty \leq \|\mathbf{W}_k\|_\infty \|\mathbf{z}_{k-1} - \tilde{\mathbf{z}}_{k-1}\|_\infty + \|\mathbf{W}_k - \tilde{\mathbf{W}}_k\|_\infty \|\tilde{\mathbf{z}}_{k-1}\|_\infty + \|\mathbf{b}_k - \tilde{\mathbf{b}}_k\|_\infty.$$

Note that $\|\tilde{\mathbf{a}}_{k-1}\|_\infty \leq (E_n + \delta_1)^{k-1}$. By induction over $k = 2, \dots, H_n$ and accounting for the total number of parameters in each layer (width products $\prod L_k$), the perturbations δ_1 across H_n layers accumulate linearly. The initial perturbation from inactive columns $(J_n - m)\delta_2$ is magnified by the depth-induced factor $(E_n + \delta_1)^{H_n - 1}$. Summing these contributions yields the desired bound. \square

B.3.1. DEFINITION OF $\tilde{M}_{n,1}(\varepsilon_n)$ AND $\tilde{M}_{n,2}(\varepsilon_n)$ IN THEOREM 5.7

- $\sigma_{0,n}^2 \leq \tilde{M}_{n,1}(\varepsilon_n)$;
- $\max\{\sigma^2, \sigma_{0,n}^2, \sigma_{1,n}^2\} \leq \tilde{M}_{n,2}(\varepsilon_n)$.

Here,

$$\tilde{M}_{n,1}(\varepsilon_n) = \min \left\{ \frac{(\delta'_n)^2}{2\tau A_n + 2 \log(4J_n L_1^2)}, \frac{(\omega'_n)^2}{2 \log(4J_n L_1^2)} \right\}, \quad (18)$$

and

$$\tilde{M}_{n,2}(\varepsilon_n) = \frac{M_n^2}{2 \left[b_1 n \varepsilon_n^2 + \log(2K_n) \right]}, \quad (19)$$

where $A_n = H_n \log n + H_n \log \bar{L} + \log\{(J_n + 1)L_1\}$,

$$\delta'_n = \frac{c_1 \varepsilon_n}{H_n J_n L_1 (\bar{L})^{2(H_n-1)} (c_0 M_n)^{H_n-1}}, \quad (20)$$

and

$$\omega'_n = \frac{c_1 \varepsilon_n}{J_n L_1 (\bar{L})^{2(H_n-1)} (c_0 E_n)^{H_n-1}}, \quad (21)$$

with c_0 and c_1 being some positive constants. In addition, $K_n = (J_n + 1)L_1 + H_n \bar{L}^2$, $\log M_n = O(\log n)$, and that for sufficiently large n , $M_n \geq E_n$.

B.3.2. PROOF OF THEOREM 5.7

We consider the specific scenario developed in Section 3. The observed data is $D_n = \{(\mathbf{x}_i(t), Y_i)\}_{i=1}^n$.

Throughout the posterior contraction analysis, we take the reference truth to be the original law

$$p^* := p_{\mu^*},$$

where the model family is indexed by $\mu_\theta(X) := F_\theta(\boldsymbol{\eta}(X))$ and the true mean is $\mu^*(X) = g^*(\langle X, \beta^* \rangle)$. Here, $p_{\mu^*}(\cdot | X)$ is the true conditional density of Y given X . Let $P_n := \{p_{\mu_\theta} : \theta \in \Theta_n\} \subset \mathcal{P}$ be a sequence of model classes, where $p_{\mu_\theta}(\cdot | X)$ is the approximate density induced by the finite-dimensional representation (3) and the sparse DNN defined in (4) and $\Theta_n := \{\theta : \|\theta\|_\infty \leq M_n, C(\theta) \leq k_0 s_n\}$ for a constant $k_0 \geq 2$. Here, $C(\theta) := |S(\theta)|$ with $S(\theta) := \{j \leq J_n : \max_{1 \leq h \leq L_1} |W_{1,hj}| \geq \delta'_n\}$.

To prove Theorem 5.7, according to Lemma B.3, it suffices to verify that for a sequence $\varepsilon_n^2 \lesssim \frac{s_n \log(J_n/s_n)}{n} + \frac{s_n (H_n \log n + \log J_n)}{n} + (H_n^{-2\alpha_1} + J_n^{-\alpha_\beta \alpha_1})^2$, the following conditions hold for all sufficiently large n :

- $\log N(\varepsilon_n, P_n, d) \leq n\varepsilon_n^2$;
- $\pi(P_n^c) \leq \exp(-bn\varepsilon_n^2)$;
- $\pi\{p_{\mu_\theta} \in \mathcal{P} : d_t(p_{\mu_\theta}, p_{\mu^*}) \leq b'\varepsilon_n^2\} \geq \exp(-b'n\varepsilon_n^2)$.

Verification of condition (a). Set

$$\delta'_n = \frac{c_1 \varepsilon_n}{H_n J_n L_1 (\bar{L})^{2(H_n-1)} (c_0 M_n)^{H_n-1}}.$$

Fix $\theta \in \Theta_n$ and let $S := S(\theta)$ with $|S| \leq k_0 s_n$. Define the truncated parameter $\theta^{(S)}$ by zeroing out non-activated columns:

$$W_{1,hg}^{(S)} := W_{1,hg} \mathbf{1}\{g \in S\}, \quad 1 \leq h \leq L_1, 1 \leq g \leq J_n,$$

and keep all remaining coordinates unchanged: $\theta_j^{(S)} := \theta_j$ for $j \in \mathcal{G}$ (\mathcal{G} includes all biases and weights beyond the first layer). Then for $g \notin S$,

$$\max_{h \leq L_1} |W_{1,hg} - W_{1,hg}^{(S)}| = \max_{h \leq L_1} |W_{1,hg}| < \delta'_n.$$

Applying Lemma B.4 with $(\delta_1, \delta_2) = (0, \delta'_n)$ yields

$$\sup_{\mathbf{x} \in [-1,1]^{J_n}} |F_{\theta}(\mathbf{x}) - F_{\theta^{(S)}}(\mathbf{x})| \leq C \varepsilon_n, \quad (22)$$

with C being some constant.

Now consider the truncated class

$$\Theta_n^{\text{trunc}}(S) := \left\{ \theta : \|\theta\|_{\infty} \leq M_n, \mathbf{W}_{1,*g} \equiv 0 \text{ for } g \notin S \right\}.$$

Set

$$\delta_{1,n} := \frac{c_2 \varepsilon_n}{H_n (k_0 s_n + 1) L_1 (\bar{L})^{2(H_n-1)} (c_0 M_n)^{H_n-1}}, \quad c_2 \in (0, 1). \quad (23)$$

Let $\tilde{\theta} \in \Theta_n^{\text{trunc}}(S)$ satisfy the coordinate-wise bounds

$$\max_{g \in S, h \leq L_1} |W_{1,hg}^{(S)} - \tilde{W}_{1,hg}| \leq \delta_{1,n}, \quad \max_{j \in \mathcal{G}} |\theta_j^{(S)} - \tilde{\theta}_j| \leq \delta_{1,n}.$$

For $g \notin S$, we have $W_{1,hg}^{(S)} = \tilde{W}_{1,hg} = 0$, hence the same bound holds with $\delta_2 = 0 \leq \delta'_n$. Therefore Lemma B.4 (with $(\delta_1, \delta_2) = (\delta_{1,n}, \delta'_n)$) and (23) give

$$\sup_{\mathbf{x} \in [-1,1]^{J_n}} |F_{\theta^{(S)}}(\mathbf{x}) - F_{\tilde{\theta}}(\mathbf{x})| \leq C \varepsilon_n. \quad (24)$$

Combining (22)–(24),

$$\sup_{\mathbf{x} \in [-1,1]^{J_n}} |F_{\theta}(\mathbf{x}) - F_{\tilde{\theta}}(\mathbf{x})| \leq C \varepsilon_n.$$

As $\mu_{\theta}(X) = F_{\theta}(\mathbf{x})$ with $\mathbf{x} = \boldsymbol{\eta}(X)$, we further have

$$\sup_{X \in \mathcal{X}} |\mu_{\theta}(X) - \mu_{\tilde{\theta}}(X)| \leq C \varepsilon_n.$$

Next, since $d^2(p, q) \leq d_0(p, q)$, it suffices to control the Kullback–Leibler divergence. For the Gaussian regression case, the KL divergence is bounded by the squared difference of mean functions. Hence,

$$d_0(p_{\mu_{\theta}}, p_{\mu_{\tilde{\theta}}}) \leq C \mathbb{E}_X [\mu_{\theta}(X) - \mu_{\tilde{\theta}}(X)]^2 \leq C' \varepsilon_n^2,$$

and therefore $d(p_{\theta}, p_{\tilde{\theta}}) \leq C'' \varepsilon_n$ for all large n . Consequently, any coordinate-wise ℓ_{∞} -net for $\Theta_n^{\text{trunc}}(S)$ induces a $c \varepsilon_n$ -net (for some constant $c > 0$) under d . Since $N(\varepsilon; P_n, d)$ is non-increasing in ε , it suffices to bound $N(c \varepsilon_n; P_n, d)$, which is of the same order.

Fix $S \subset \{1, \dots, J_n\}$ with $m := |S| \leq k_0 s_n$ and let $K_{\text{deep}} := |\mathcal{G}| \leq H_n \bar{L}^2$. Discretise (i) the $m L_1$ active first-layer weights and (ii) the K_{deep} deep-layer coordinates on a uniform grid over $[-M_n, M_n]$ with mesh width $\delta_{1,n}$. Let $R_n := \left\lceil \frac{2M_n}{\delta_{1,n}} \right\rceil$. By product covering, there exists an $c \varepsilon_n$ -net $\mathcal{N}(S)$ of $\{\theta \in \Theta_n^{\text{trunc}}(S)\}$ under d such that $|\mathcal{N}(S)| \leq R_n^{m L_1 + K_{\text{deep}}}$.

Since $m \leq k_0 s_n$,

$$\sum_{m=0}^{k_0 s_n} \binom{J_n}{m} \leq \left(\frac{e J_n}{k_0 s_n} \right)^{k_0 s_n}.$$

Let $\mathcal{N} := \bigcup_{|S| \leq k_0 s_n} \mathcal{N}(S)$. For any $\theta \in \Theta_n$, letting $S = S(\theta)$, the truncation bridge and the net $\mathcal{N}(S)$ yield some $\tilde{\theta} \in \mathcal{N}(S) \subset \mathcal{N}$ such that $d(p_\theta, p_{\tilde{\theta}}) \leq \varepsilon_n$. Therefore, for the constant $c > 0$ above,

$$\begin{aligned} \log N(c\varepsilon_n; P_n, d) &\leq k_0 s_n \log \frac{e J_n}{k_0 s_n} + (k_0 s_n L_1 + K_{\text{deep}}) \log R_n \\ &\leq k_0 s_n \log \frac{e J_n}{k_0 s_n} + (k_0 s_n L_1 + H_n \bar{L}^2) \log \frac{2M_n}{\delta_{1,n}}. \end{aligned}$$

Since $N(\varepsilon; P_n, d)$ is non-increasing in ε , $\log N(\varepsilon_n; P_n, d) \leq \log N(c\varepsilon_n; P_n, d)$. By $\log M_n = O(\log n)$ and $\log(1/\varepsilon_n) = O(\log n)$, and noting that k_0 is fixed and $k_0 s_n \leq J_n$, we obtain

$$\log N(\varepsilon_n; P_n, d) \lesssim s_n \log \frac{e J_n}{s_n} + [s_n L_1 + H_n \bar{L}^2] \left(H_n \log n + H_n \log \bar{L} + \log(J_n L_1) \right).$$

By the rate condition of ε_n , the right-hand side is $O(n\varepsilon_n^2)$, hence $\log N(\varepsilon_n; P_n, d) \leq n\varepsilon_n^2$ for all large n , verifying condition (a).

Verification of condition (b). By the definition of Θ_n , we have

$$\Pi(\Theta_n^c) \leq T_{1,n} + T_{2,n}, \quad T_{1,n} := \Pi(\|\boldsymbol{\theta}\|_\infty > M_n), \quad T_{2,n} := \Pi(C(\boldsymbol{\theta}) > k_0 s_n).$$

Note that, under the induced prior on densities,

$$\Pi(P_n^c) = \Pi\{\boldsymbol{\theta} \notin \Theta_n\} = \Pi(\Theta_n^c).$$

Denote $\sigma_{\max}^2 = \max\{\sigma^2, \sigma_{0,n}^2, \sigma_{1,n}^2\}$ and $K_n = (J_n + 1)L_1 + H_n \bar{L}^2$. For every coordinate θ_j , $\Pr(|\theta_j| > M_n) \leq 2 \exp(-M_n^2/2\sigma_{\max}^2)$. With the condition (19) on σ_{\max}^2 and by the union bound, we have

$$T_{1,n} \leq 2K_n \exp\left(-\frac{M_n^2}{2\sigma_{\max}^2}\right) \leq \exp(-b_1 n\varepsilon_n^2).$$

For each column g , define

$$I_g := \mathbf{1}\left\{ \max_{1 \leq h \leq L_1} |W_{1,hg}| \geq \delta'_n \right\}, \quad C(\boldsymbol{\theta}) = \sum_{g=1}^{J_n} I_g.$$

Under the specific prior, the indicators $\{I_g\}_{g=1}^{J_n}$ are i.i.d. Bernoulli (p_n) with

$$p_n := \Pr(I_g = 1) = (1 - \lambda_n)p_{0,n} + \lambda_n p_{1,n} \leq p_{0,n} + \lambda_n, \quad (25)$$

where

$$\begin{aligned} p_{0,n} &:= \Pr\left(\max_{1 \leq h \leq L_1} |Z_h| \geq \delta'_n \right), & Z_h &\stackrel{\text{i.i.d.}}{\sim} N(0, \sigma_{0,n}^2), \\ p_{1,n} &:= \Pr\left(\max_{1 \leq h \leq L_1} |W_h| \geq \delta'_n \right), & W_h &\stackrel{\text{i.i.d.}}{\sim} N(0, \sigma_{1,n}^2). \end{aligned}$$

By the union bound and Gaussian tails,

$$p_{0,n} \leq 2L_1 \exp\left(-\frac{(\delta'_n)^2}{2\sigma_{0,n}^2}\right), \quad p_{1,n} \leq 1.$$

Under assumption (18) for $\sigma_{0,n}^2$, we have

$$\frac{(\delta'_n)^2}{2\sigma_{0,n}^2} \geq \tau A_n + \log(4J_n L_1^2),$$

with $A_n = H_n \log n + H_n \log \bar{L} + \log\{(J_n + 1)L_1\}$, and hence

$$p_{0,n} \leq 2L_1 \exp\left(-\frac{(\delta'_n)^2}{2\sigma_{0,n}^2}\right) \leq 2L_1 \exp\{-\tau A_n - \log(4J_n L_1^2)\} = \frac{1}{2J_n L_1} e^{-\tau A_n}. \quad (26)$$

Therefore $J_n p_{0,n} \leq \frac{1}{2L_1} e^{-\tau A_n}$, which is $o(s_n)$ and in particular implies $J_n p_{0,n} \leq \frac{1}{4} k_0 s_n$ for all large n . Moreover, under Assumption 5.5, we have $J_n \lambda_n \lesssim [(n\bar{L})^{H_n} (J_n + 1)L_1]^{-\tau'}$, so for all large n ,

$$J_n \lambda_n \leq \frac{1}{4} k_0 s_n.$$

Combining the last two displays yields

$$J_n p_n \leq J_n (p_{0,n} + \lambda_n) \leq \frac{1}{2} k_0 s_n.$$

Let $q_n := k_0 s_n / J_n$ and assume $q_n \leq 1/2$ for all large n . Since $\{I_g\}_{g=1}^{J_n}$ are i.i.d. Bernoulli(p_n), we have

$$C(\boldsymbol{\theta}) = \sum_{g=1}^{J_n} I_g \sim \text{Bin}(J_n, p_n).$$

Under the above bounds, we have $p_n \leq q_n/2$, hence $q_n > p_n$. Applying Zubkov & Serov (2013, Theorem 1) to $X \sim \text{Bin}(J_n, p_n)$ with $k = \lfloor J_n q_n \rfloor - 1$ yields

$$\Pr\{C(\boldsymbol{\theta}) \geq k_0 s_n\} \leq 1 - \Phi\left(\sqrt{2J_n H(p_n, q_n)}\right),$$

where

$$H(p_n, q_n) = q_n \log \frac{q_n}{p_n} + (1 - q_n) \log \frac{1 - q_n}{1 - p_n} = \text{KL}(q_n \| p_n).$$

Using the standard Gaussian tail bound $1 - \Phi(t) \leq e^{-t^2/2}$ for $t > 0$, we obtain

$$\Pr\{C(\boldsymbol{\theta}) \geq k_0 s_n\} \leq \exp\{-J_n \text{KL}(q_n \| p_n)\}.$$

Moreover, since $p_n \leq q_n/2$ and $\log(q_n/p_n) \rightarrow \infty$ in our regime, the negative term $(1 - q_n) \log\{(1 - q_n)/(1 - p_n)\}$ is negligible compared to $q_n \log(q_n/p_n)$, and in particular for all sufficiently large n ,

$$\text{KL}(q_n \| p_n) \geq \frac{1}{2} q_n \log \frac{q_n}{p_n}.$$

Therefore,

$$\Pr\{C(\boldsymbol{\theta}) \geq k_0 s_n\} \leq \exp\left\{-c k_0 s_n \log \frac{q_n}{p_n}\right\}$$

for some absolute constant $c > 0$.

Moreover, under Assumption 5.5 and (25) and (26), we can ensure $p_n \lesssim e^{-\tau A_n} / J_n$ for some $\tau > 0$, so that

$$\log \frac{q_n}{p_n} \gtrsim \tau A_n + \log(k_0 s_n) \gtrsim A_n \quad \text{for all large } n.$$

Therefore,

$$-\log \Pr\{C(\boldsymbol{\theta}) \geq k_0 s_n\} \gtrsim k_0 s_n A_n.$$

Then, under Assumption 5.6, we have $n\varepsilon_n^2 \lesssim s_n A_n$, and thus for some $b_2 > 0$,

$$T_{2,n} = \Pi\{C(\boldsymbol{\theta}) > k_0 s_n\} \leq \exp(-b_2 n\varepsilon_n^2),$$

verifying condition (b).

Verification of condition (c). We check condition (c) for $t = 1$. Consider the set

$$\mathcal{A}_n = \left\{ \boldsymbol{\theta} : \max_{g \in S_{J_n}^*} \max_{h \leq L_1} |W_{1,hg} - W_{1,hg}^*| \leq \omega_n, \max_{g \notin S_{J_n}^*} \max_{h \leq L_1} |W_{1,hg}| \leq \omega'_n, \|\boldsymbol{\theta}_G - \boldsymbol{\theta}_G^*\|_\infty \leq \omega_n \right\},$$

where $\omega_n = \frac{c_1 \varepsilon_n}{[H_n(s_n+1)L_1(\bar{L})^2(H_n-1)(c_0 E_n)^{H_n-1}]}$ and ω'_n are defined in (20) and (21), and $\boldsymbol{\theta}^*$ is the network parameter vector of the DNN $F_{\boldsymbol{\theta}^*}$ obtained in Theorem 5.4. If $\boldsymbol{\theta} \in \mathcal{A}_n$, then by Lemma B.4 we have

$$\sup_{X \in \mathcal{X}} |\mu_{\boldsymbol{\theta}}(X) - \mu_{\boldsymbol{\theta}^*}(X)| = \sup_{\mathbf{x} \in [-1,1]^{J_n}} |F_{\boldsymbol{\theta}}(\mathbf{x}) - F_{\boldsymbol{\theta}^*}(\mathbf{x})| \leq 3c_1 \varepsilon_n,$$

where $\mathbf{x} = \boldsymbol{\eta}(X)$ and $\mu_{\boldsymbol{\theta}}(X) = F_{\boldsymbol{\theta}}(\boldsymbol{\eta}(X))$. Define

$$\tilde{\xi}_n := \inf_{\boldsymbol{\theta} : \text{supp}_{\text{col}}(\boldsymbol{\theta}) = S_{J_n}^*, \|\boldsymbol{\theta}\|_\infty \leq E_n} \sup_{X \in \mathcal{X}} |\mu_{\boldsymbol{\theta}}(X) - \mu^*(X)|.$$

Then, Theorem 5.4 gives $\tilde{\xi}_n \lesssim H_n^{-2\alpha_1} + J_n^{-\alpha_\beta \alpha_1}$.

Since

$$\sup_{X \in \mathcal{X}} |\mu_{\boldsymbol{\theta}^*}(X) - \mu^*(X)| \leq \tilde{\xi}_n,$$

we have,

$$\sup_{X \in \mathcal{X}} |\mu_{\boldsymbol{\theta}}(X) - \mu^*(X)| \leq 3c_1 \varepsilon_n + \tilde{\xi}_n.$$

For normal models, we obtain

$$d_1(p_{\mu_{\boldsymbol{\theta}}}, p_{\mu^*}) \leq C(1 + o(1)) \mathbb{E}_X [\mu_{\boldsymbol{\theta}}(X) - \mu^*(X)]^2 \leq C(1 + o(1)) (3c_1 \varepsilon_n + \tilde{\xi}_n)^2, \quad \text{if } \boldsymbol{\theta} \in \mathcal{A}_n,$$

for some constant C . Under Assumption 5.6, we have $n\varepsilon_n^2 \geq M_0 n \tilde{\xi}_n^2$ for large M_0 . Thus for any small $b' > 0$, condition (c) holds as long as c_1 is sufficiently small, and the prior satisfies $-\log \Pi(\mathcal{A}_n) \leq b' n \varepsilon_n^2$.

Let $S_{J_n}^* \subset \{1, \dots, J_n\}$ be the true active column set with $|S_{J_n}^*| = s_n$, and define the configuration $\boldsymbol{\gamma}^*$ by $\gamma_g^* = \mathbf{1}\{g \in S_{J_n}^*\}$. Write $K_{\text{deep}} := |\mathcal{G}| \leq H_n \bar{L}^2$.

Since columns are independent under the hierarchical prior and (γ_g) are i.i.d.,

$$\Pi(\mathcal{A}_n) \geq \Pi(\boldsymbol{\gamma} = \boldsymbol{\gamma}^*) \Pi(\mathcal{A}_n | \boldsymbol{\gamma} = \boldsymbol{\gamma}^*).$$

To bound $\Pi(\mathcal{A}_n)$ from below, we consider the event where the selection indicators match the target indices exactly, i.e., $\gamma_g = 1$ if $g \in S_{J_n}^*$ and $\gamma_g = 0$ otherwise.

(i) Consider $\Pi(\boldsymbol{\gamma} = \boldsymbol{\gamma}^*)$.

$$\Pi(\boldsymbol{\gamma} = \boldsymbol{\gamma}^*) = \lambda_n^{s_n} (1 - \lambda_n)^{J_n - s_n}, \quad \Rightarrow \quad -\log \Pi(\boldsymbol{\gamma} = \boldsymbol{\gamma}^*) \leq s_n \log \frac{1}{\lambda_n} + (J_n - s_n) \lambda_n.$$

Under Assumption 5.5, $(J_n - s_n) \lambda_n = o(n \varepsilon_n^2)$ and $s_n \log(1/\lambda_n) \lesssim s_n \{H_n \log n + H_n \log \bar{L} + \log(J_n L_1)\}$.

(ii) Consider $\Pi(\mathcal{A}_n | \boldsymbol{\gamma} = \boldsymbol{\gamma}^*)$.

For $X \sim N(0, \sigma^2)$ and any $|a| \leq E_n$,

$$\Pr(|X - a| \leq \omega) \geq 2\omega \cdot \inf_{|u-a| \leq \omega} \phi(u; 0, \sigma^2) \geq c \frac{\omega}{\sigma} \exp\left(-\frac{(E_n + \omega)^2}{2\sigma^2}\right),$$

hence

$$-\log \Pr(|X - a| \leq \omega) \lesssim \log \frac{\sigma}{\omega} + \frac{(E_n + 1)^2}{2\sigma^2}.$$

Applying this bound to the active first-layer weights ($s_n L_1$ coordinates with slab variance $\sigma_{1,n}^2$) and to the deep parameters (K_{deep} coordinates with variance σ^2), we obtain

$$\begin{aligned} -\log \Pi(\mathcal{A}_n \mid \gamma = \gamma^*) &\leq C \left[s_n L_1 \left\{ \log \frac{\sigma_{1,n}}{\omega_n} + \frac{(E_n + 1)^2}{2\sigma_{1,n}^2} \right\} + K_{\text{deep}} \left\{ \log \frac{\sigma}{\omega_n} + \frac{(E_n + 1)^2}{2\sigma^2} \right\} \right] \\ &\quad - \log \Pi \left(\max_{g \notin S_{J_n}^*} \max_{h \leq L_1} |W_{1,hg}| \leq \omega'_n \mid \gamma_g = 0 \forall g \notin S_{J_n}^* \right). \end{aligned}$$

For the inactive part, by (19) and (21), we have

$$\frac{(\omega'_n)^2}{2\sigma_{0,n}^2} \geq \log(4J_n L_1^2),$$

so for $Z \sim N(0, \sigma_{0,n}^2)$,

$$\Pr(|Z| > \omega'_n) \leq 2 \exp\left(-\frac{(\omega'_n)^2}{2\sigma_{0,n}^2}\right) \leq \frac{1}{2J_n L_1^2}.$$

Hence, for each (g, h) with $g \notin S_{J_n}^*$,

$$\Pr(|W_{1,hg}| \leq \omega'_n \mid \gamma_g = 0) \geq 1 - \frac{1}{2J_n L_1^2}.$$

By independence over (g, h) ,

$$\Pi \left(\max_{g \notin S_{J_n}^*} \max_{h \leq L_1} |W_{1,hg}| \leq \omega'_n \mid \gamma_g = 0 \forall g \notin S_{J_n}^* \right) \geq \left(1 - \frac{1}{2J_n L_1^2}\right)^{(J_n - s_n)L_1} \geq e^{-1}$$

for all large n .

Combining the above bounds and using $K_n \leq H_n \bar{L}^2$ and $\log(1/\omega_n) = O(H_n \log n + H_n \log \bar{L} + \log(s_n L_1))$, we conclude that

$$-\log \Pi(\mathcal{A}_n) \leq C' \left\{ s_n \log \frac{1}{\lambda_n} + [s_n L_1 + H_n \bar{L}^2] (H_n \log n + H_n \log \bar{L} + \log(s_n L_1)) \right\} \leq b' n \varepsilon_n^2,$$

where the last inequality follows from the rate condition and the hyper-parameter bounds in Assumption 5.5. Consequently, $\Pi(\mathcal{A}_n) \geq \exp(-b' n \varepsilon_n^2)$, verifying condition (c).

B.4. Selection consistency (Theorem 5.9)

Denote $q_j = \Pi(r_j = 1 \mid D_n) = \mathbb{E}(r_j \mid D_n)$ and $A_n(\varepsilon_n) = \left\{ \theta : d(p_{\mu_\theta}, p_{\mu^*}) \geq \varepsilon_n \right\}$.

B.4.1. PROOF OF THEOREM 5.9

Fix $j \in \{1, \dots, J_n\}$. By the definition of q_j , we have

$$|q_j - e_j^*| = \left| \mathbb{E}((\gamma_j - e_j^*) \mid D_n) \right| \leq \mathbb{E}(|\gamma_j - e_j^*| \mid D_n).$$

Split according to $A_n(4\varepsilon_n)$:

$$\mathbb{E}(|\gamma_j - e_j^*| \mid D_n) \leq \mathbb{E}\left[|\gamma_j - e_j^*| \mathbf{1}\{\theta \notin A_n(4\varepsilon_n)\} \mid D_n\right] + \mathbb{E}\left[|\gamma_j - e_j^*| \mathbf{1}\{\theta \in A_n(4\varepsilon_n)\} \mid D_n\right].$$

Since $|\gamma_j - e_j^*| \leq 1$, the second term is bounded by $\Pi(A_n(4\varepsilon_n) \mid D_n)$, while the first term is controlled by $\rho_n(4\varepsilon_n)$ in Assumption 5.8. Taking the maximum over j gives

$$\max_j |q_j - e_j^*| \leq \rho_n(4\varepsilon_n) + \Pi(A_n(4\varepsilon_n) \mid D_n) \xrightarrow{P} 0.$$

Then based on Theorem 2.3 stated in Sun et al. (2022), with an appropriate choice of prior hyperparameters, the estimated $\hat{q}_j = Pr(r_j = 1|\hat{\theta})$ based on the MAP estimate $\hat{\theta}$ and q_j are approximately the same as $n \rightarrow \infty$. Thus, \hat{q}_j is also a consistent estimator of e_j^* , which proves (i). Parts (ii) and (iii) follow immediately from (i).

To prove (iv), recall that the estimated active region on the original domain is $\hat{\Omega} := \bigcup_{j \in \hat{S}_{1/2}} I_j$, and the population (truncated) active region at resolution J_n is $\Omega_{J_n}^* = \bigcup_{j \in S_{J_n}^*} I_j$. By Parts (i)–(iii), $Pr(\hat{S}_{1/2} = S_{J_n}^*) \rightarrow 1$, hence also $Pr(\hat{\Omega} = \Omega_{J_n}^*) \rightarrow 1$. Therefore, it suffices to show $|\Omega_{J_n}^* \Delta \Omega^*| \rightarrow 0$.

By the triangle inequality for symmetric differences,

$$|\Omega_{J_n}^* \Delta \Omega^*| \leq |\Omega_{J_n}^* \Delta \Omega^*(2\kappa_{J_n})| + |\Omega^*(2\kappa_{J_n}) \Delta \Omega^*|. \quad (27)$$

For the first term, Lemma B.1(v) gives

$$|\Omega_{J_n}^* \Delta \Omega^*(2\kappa_{J_n})| \leq |\Omega^*(\kappa_{J_n}) \setminus \Omega^*(2\kappa_{J_n})| + \left| \Omega_{J_n}^*(\kappa_{J_n})^{+c_{\text{loc}}\Delta_{J_n}} \setminus \Omega^*(\kappa_{J_n}) \right|.$$

The first summand is controlled by Assumption 5.2, since $\Omega^*(\kappa_{J_n}) \setminus \Omega^*(2\kappa_{J_n}) \subseteq \{t \in \Omega^* : |\beta^*(t)| \leq 2\kappa_{J_n}\}$ and $2\kappa_{J_n} \downarrow 0$, hence $|\Omega^*(\kappa_{J_n}) \setminus \Omega^*(2\kappa_{J_n})| \leq |\{t \in \Omega^* : |\beta^*(t)| \leq 2\kappa_{J_n}\}| \rightarrow 0$.

For the second summand, we relate $\Omega_{J_n}^*(\kappa)$ to $\Omega^*(\kappa)$ via a Δ_{J_n} -enlargement. Indeed, by definition $\Omega^*(\kappa) \subseteq \Omega_{J_n}^*(\kappa)$; moreover, since each spline support interval I_j has diameter at most Δ_{J_n} , if $t \in I_j$ for some j with $I_j \cap \Omega^*(\kappa) \neq \emptyset$, then there exists $s \in I_j \cap \Omega^*(\kappa)$ such that $|t - s| \leq \text{diam}(I_j) \leq \Delta_{J_n}$, implying $\Omega_{J_n}^*(\kappa) \subseteq \Omega^*(\kappa)^{+\Delta_{J_n}}$. Consequently,

$$\Omega_{J_n}^*(\kappa)^{+c_{\text{loc}}\Delta_{J_n}} \subseteq (\Omega^*(\kappa)^{+\Delta_{J_n}})^{+c_{\text{loc}}\Delta_{J_n}} = \Omega^*(\kappa)^{+(c_{\text{loc}}+1)\Delta_{J_n}},$$

and hence

$$\left| \Omega_{J_n}^*(\kappa_{J_n})^{+c_{\text{loc}}\Delta_{J_n}} \setminus \Omega^*(\kappa_{J_n}) \right| \leq \left| \Omega^*(\kappa_{J_n})^{+(c_{\text{loc}}+1)\Delta_{J_n}} \setminus \Omega^*(\kappa_{J_n}) \right|.$$

Since $\Omega^*(\kappa_{J_n})$ is a finite union of intervals, its boundary has finite cardinality; therefore there exists $C_\partial > 0$ such that for all $\delta > 0$, $|\Omega^*(\kappa_{J_n})^{+\delta} \setminus \Omega^*(\kappa_{J_n})| \leq C_\partial \delta$. Taking $\delta = (c_{\text{loc}} + 1)\Delta_{J_n}$ and using $\Delta_{J_n} \asymp J_n^{-1} \rightarrow 0$ yields $|\Omega_{J_n}^*(\kappa_{J_n})^{+c_{\text{loc}}\Delta_{J_n}} \setminus \Omega^*(\kappa_{J_n})| \rightarrow 0$. This shows $|\Omega_{J_n}^* \Delta \Omega^*(2\kappa_{J_n})| \rightarrow 0$.

For the second term in (27), note that $\Omega^* \setminus \Omega^*(2\kappa_{J_n}) \subseteq \{t \in \Omega^* : |\beta^*(t)| \leq 2\kappa_{J_n}\}$, and hence

$$|\Omega^*(2\kappa_{J_n}) \Delta \Omega^*| = |\Omega^* \setminus \Omega^*(2\kappa_{J_n})| \leq |\{t \in \Omega^* : |\beta^*(t)| \leq 2\kappa_{J_n}\}| \rightarrow 0$$

by Assumption 5.2. Combining the above bounds gives $|\Omega_{J_n}^* \Delta \Omega^*| \rightarrow 0$, and therefore

$$|\hat{\Omega} \Delta \Omega^*| \leq |\hat{\Omega} \Delta \Omega_{J_n}^*| + |\Omega_{J_n}^* \Delta \Omega^*| \xrightarrow{P} 0,$$

which completes the proof of (iv).

C. Detailed simulation settings and additional simulation results

Following the functional-covariate generation mechanism in AdaFNN, we generate $X_i(\cdot)$ from a truncated cosine expansion on $\mathcal{T} = [0, 1]$. Let $\phi_1(t) \equiv 1$ and $\phi_k(t) = \sqrt{2} \cos((k-1)\pi t)$ for $k = 2, \dots, K$ with $K = 50$, and set $X_i(t) = \sum_{k=1}^K c_{ik} \phi_k(t)$. We draw $c_{ik} = z_k r_{ik}$ with $r_{ik} \stackrel{\text{i.i.d.}}{\sim} \text{Unif}(-\sqrt{3}, \sqrt{3})$ and $z_1 = 20$, $z_2 = z_3 = 15$, and $z_k = 1$ for $k \geq 4$. We observe each curve on a discrete grid over $[0, 1]$.

We consider three localized settings for $\beta(\cdot)$, which we label as *Simple*, *Medium*, and *Complex* according to increasing difficulty in region recovery. Let $T(t; a, b) := (t-a)(b-t)\mathbf{1}\{t \in [a, b]\}$ and let $\tilde{T}(t; a, b)$ denote its normalized version on $[a, b]$ (so that $\max_{t \in [a, b]} \tilde{T}(t; a, b) = 1$). Thus, on each active interval, $\beta(\cdot)$ has a smooth quadratic bump that vanishes at the endpoints, and multiple active intervals are represented by sums over disjoint bumps. Specifically, we use: (i) (**Simple**) a single centered bump on $[0.4, 0.6]$, $\beta(t) = 5\tilde{T}(t; 0.4, 0.6)$; (ii) (**Medium**) a single boundary-adjacent bump on $[0.1, 0.3]$, $\beta(t) = 5\tilde{T}(t; 0.1, 0.3)$; and (iii) (**Complex**) two separated narrow bumps with within-region oscillation. Let $W = [a_1, b_1] \cup [a_2, b_2]$ with $(a_1, b_1) = (0.05, 0.15)$ and $(a_2, b_2) = (0.75, 0.85)$, and set $\beta(t) = 2.5 \sum_{m=1}^2 \tilde{T}(t; a_m, b_m) \sin(2\pi(t + 0.1))$. The shapes of the three $\beta(t)$ types are illustrated in Figure 6.

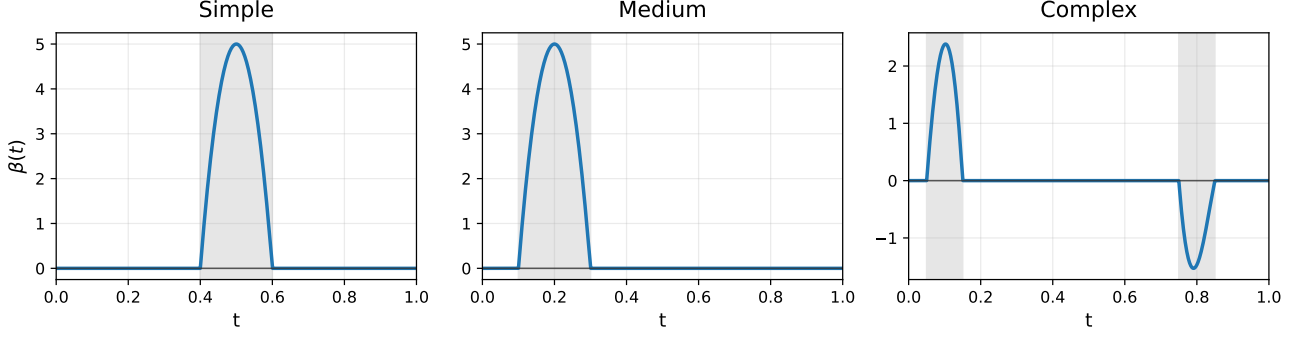


Figure 6. Illustration of the three types of coefficient functions $\beta(t)$ used in simulations: Simple (single interior bump), Medium (single boundary bump), and Complex (two separated oscillating bumps).

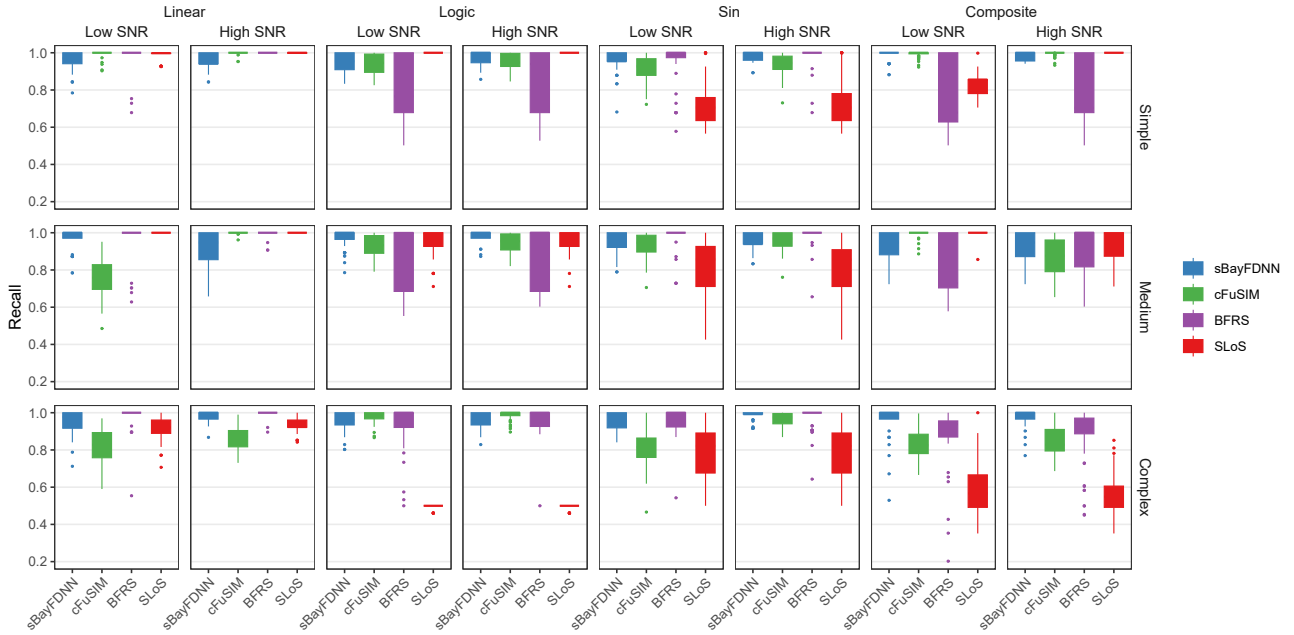


Figure 7. Recall values across g functions, SNR settings, and $\beta(t)$ scenarios.

To vary the nonlinearity of the response mechanism, we consider four choices of the link function g^* with increasing complexity: (i) linear $g^*(u) = u$; (ii) logistic-type $g^*(u) = \{1 + \exp(u)\}^{-1}$; (iii) sinusoidal $g^*(u) = \sin(u)$; and (iv) a composite link $g^*(u) = \tanh(u) + \sin(4u) \exp(-0.01u^2)$.

Finally, given a draw of $X_i(\cdot)$ and a choice of (β, g^*) , we generate the response as

$$Y_i = g^* \left(\int_0^1 X_i(t) \beta(t) dt \right) + \varepsilon_i, \quad \varepsilon_i \stackrel{\text{i.i.d.}}{\sim} \mathcal{N}(0, \sigma_\varepsilon^2).$$

To make noise levels comparable across settings, we calibrate additive Gaussian noise by a target signal-to-noise ratio, $\text{SNR} = \text{Var}(\text{signal})/\text{Var}(\text{noise})$. In all simulations, the latent curves $X_i(\cdot)$ generate the responses above, but the learning algorithms observe only discretely sampled noisy curves obtained by adding i.i.d. Gaussian measurement noise at $\text{SNR} = 10$ on the observation grid. The response noise variance σ_ε^2 is chosen so that the resulting responses attain the target response SNR (we consider $\text{SNR} \in \{5, 10\}$) in each scenario. When required, we apply a denoising step to the noisy curve observations before constructing spline features. For each scenario, we simulate 100 replicates and summarize the results in Figures 2, 4, 7, and 8.

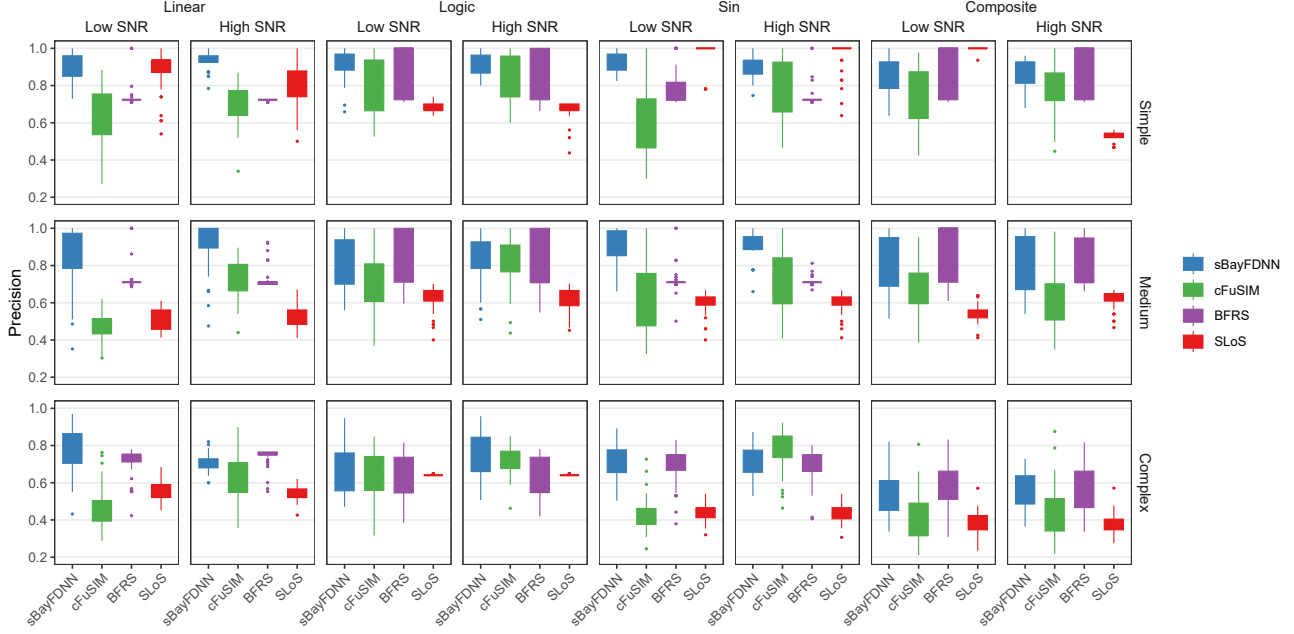


Figure 8. Precision values across g functions, SNR settings, and $\beta(t)$ scenarios.

D. Details for the Real-world Datasets

Implementation details. Relative to the simulation defaults in Appendix A.1, we keep the same network architecture and use mini-batch size 32. For smaller-sample real datasets, we recommend a less aggressive first-layer sparsification prior to mitigate underfitting; accordingly, we use $(\lambda_n, \sigma_{0,n}^2, \sigma_{1,n}^2) = (10^{-1}, 10^{-5}, 5 \times 10^{-2})$ for Tecator, Bike, and IHPC. (Unless otherwise stated, other hyperparameters follow Appendix A.1.)

ECG. The ECG dataset is from the EchoNext dataset on PhysioNet (Elias & Finer, 2025; Goldberger et al., 2000) and downloaded from <https://physionet.org/content/echonext/1.1.0/>. To reduce phase variability, we detect R-peaks and align each waveform to the detected R-peak, extract a fixed-length beat-centered window, and resample it to a common grid of length $L = 256$ at 250 Hz, following standard ECG preprocessing practice (Kachuee et al., 2018; Makowski et al., 2021). To better approximate an i.i.d. sample, we remove repeated measurements from the same subject; after deduplication, the final sample sizes are 26,192/4,618/5,434 for train/validation/test, equal to the numbers of unique patients in each split. The window length is selected using the training split only by screening candidate pre/post windows and choosing the configuration that minimizes variability of the aligned R-peak location across subjects (trimmed standard deviation below 0.03 on the normalized phase), which yields a symmetric window of 0.3 s before and 0.3 s after the R-peak. To adjust for scalar covariates, we residualize the response by fitting an OLS regression on the training split (age, sex, acquisition year, location setting, and race/ethnicity) and applying the fitted adjustment to validation/test splits. For ECG, we use a higher-capacity network (7 hidden layers of width 512; total depth 8) trained with mini-batch size 512 and learning rate 5×10^{-4} ; we consider $\mathcal{J} = \{180, 200, 220\}$ and use B-splines of degree 8 to accommodate the larger sample size and sharply localized QRS morphology.

To assess region identification, we define silver-standard intervals on the original domains and then map them to the normalized domain $\mathcal{T} = [0, 1]$ induced by our fixed-window. For ECG, we use a 120 ms window (Yu et al., 2003; Hummel et al., 2009) centered at the R peak, i.e., $[-0.06, 0.06]$ seconds relative to the R peak, as a silver-standard proxy for the QRS complex extent.

Tecator. The Tecator dataset is downloaded from <https://lib.stat.cmu.edu/datasets/tecator>. It contains near-infrared absorbance spectra of 240 meat samples measured on 100 wavelength channels ranging from 850 nm to 1,050 nm, together with moisture (water), fat and protein percentages determined by analytic chemistry. We use water as the response and follow the official split (129 training, 43 monitoring/validation, and 43 testing samples). Relative to the simulation defaults in Appendix A.1, we keep the same network architecture but use mini-batch size 32. We use $\mathcal{J} = \{80, 100, 120\}$. We use

the water-related absorption band around 970–980 nm (van Kollenburg et al., 2021) and define the silver-standard wavelength interval as $[965, 985]$ nm. The interval is then mapped to the normalized domain $\mathcal{T} = [0, 1]$ via wavelength normalization.

Bike. We use the Bike Sharing dataset (Fanaee-T, 2013) in its hourly-resolution form and represent each day as a functional observation with $T = 24$ equally spaced time points on $\mathcal{T} = [0, 1]$. The dataset can be obtained from <https://archive.ics.uci.edu/dataset/275/bike%2Bsharing%2Bdataset>. We define the response as the total demand over the next 7 days and adopt a chronological train/validation/test split with sample sizes 453/97/98 (total $N = 648$), covering the date range 2011-01-16 to 2012-12-30 (train end: 2012-06-12; validation end: 2012-09-17). We use $\mathcal{J} = \{8, 10, 12, 14\}$.

IHPC. We use the Individual Household Electric Power Consumption (IHPC) dataset from the UCI Machine Learning Repository <https://archive.ics.uci.edu/dataset/235/individual+household+electric+power+consumption> (Hebrail & Berard, 2006). We use the minute-averaged global active power trajectory as the functional input, yielding daily curves of length $T = 1440$ on $\mathcal{T} = [0, 1]$. After restricting to complete days and constructing next-day prediction pairs, we obtain $N = 1290$ samples and use a chronological train/validation/test split with sample sizes 672/329/289, spanning 2006-12-17 to 2010-11-24. We use $\mathcal{J} = \{15, 20, 30, 40\}$.

Algorithm 1: Sparse DNN elicitation with projection-size selection

Input: $\mathcal{D}_{\text{tr}} = \{(X_i, Y_i)\}_{i=1}^{n_{\text{tr}}}$, $\mathcal{D}_{\text{va}} = \{(X_i, Y_i)\}_{i=1}^{n_{\text{va}}}$; candidate projection dimensions $\mathcal{J} = \{J_1, \dots, J_M\}$; basis specification for $\{B_j(t)\}_{j \geq 1}$; random restarts R ; hyperparameters $\sigma_{0,n}^2, \sigma_{1,n}^2, \sigma^2, \lambda_n$; noise variance σ_ε^2 ; Crit $\in \{\text{evidence, val}\}$.

Output: Selected projection dimension J^* , final MAP parameter $\hat{\theta}$, and selected feature mask $\hat{\gamma}$.

foreach $J \in \mathcal{J}$ **do**

Step 0 (projection). Construct $\{B_1(t), \dots, B_J(t)\}$ and compute $\eta_J(X)$ for all $(X, Y) \in \mathcal{D}_{\text{tr}} \cup \mathcal{D}_{\text{va}}$;

for $r = 1, \dots, R$ **do**

Step 1 (initialize). Randomly initialize θ ;

Step 2 (MAP training). Obtain

$$\hat{\theta}_{J,r} \in \arg \min_{\theta} \mathcal{L}_{n,J}(\theta) = \frac{1}{2\sigma_\varepsilon^2} \sum_{(X_i, Y_i) \in \mathcal{D}_{\text{tr}}} \left(Y_i - f_{\theta}(\eta_J(X_i)) \right)^2 - \log \pi(\theta).$$

Step 3 (validation score). Set $v_{J,r} := \text{MSE}(\hat{\theta}_{J,r}; \mathcal{D}_{\text{va}})$;

Step 4 (feature mask and evidence surrogate). Let $\widehat{\mathbf{W}}_{J,r}^{(1)} \in \mathbb{R}^{w \times J}$ be the first-layer weight matrix in $\hat{\theta}_{J,r}$. For $j = 1, \dots, J$, set

$$\gamma_{J,r,j} = \mathbb{1} \left(\left\| \widehat{\mathbf{W}}_{J,r,;j}^{(1)} \right\|_2^2 > \tau_n \right), \quad \tau_n := \frac{\log((1 - \lambda_n)/\lambda_n) + \frac{w}{2} \log(\sigma_{1,n}^2/\sigma_{0,n}^2)}{\frac{1}{2\sigma_{0,n}^2} - \frac{1}{2\sigma_{1,n}^2}}.$$

Denote $\hat{\gamma}_{J,r} := (\gamma_{J,r,1}, \dots, \gamma_{J,r,J})^\top$ and construct the evidence surrogate $\hat{\theta}_{J,r}^s$ by replacing $\widehat{\mathbf{W}}_{J,r}^{(1)}$ with $\widehat{\mathbf{W}}_{J,r}^{(1)} \text{diag}(\hat{\gamma}_{J,r})$ (used only for evidence computation);

Step 5 (evidence score; post-sparsification). Compute $\ell_{J,r} := \log \text{Ev}(\hat{\theta}_{J,r}^s; \mathcal{D}_{\text{tr}})$;

Step 6 (aggregate over restarts). Set $\bar{\ell}_J := R^{-1} \sum_{r=1}^R \ell_{J,r}$ and $\bar{v}_J := R^{-1} \sum_{r=1}^R v_{J,r}$;

Step 7 (select J). **if** Crit = *evidence* **then**

$J^* \in \arg \max_{J \in \mathcal{J}} \bar{\ell}_J$;

else

$J^* \in \arg \min_{J \in \mathcal{J}} \bar{v}_J$;

Step 8 (select final restart at \hat{J}). $r^* \in \arg \min_{r \in \{1, \dots, R\}} v_{J^*,r}$; $\hat{\theta} \leftarrow \hat{\theta}_{J^*,r^*}$;

$\hat{\gamma} \leftarrow \hat{\gamma}_{J^*,r^*}$;

return $(J^*, \hat{\theta}, \hat{\gamma})$.